JGR Solid Earth

RESEARCH ARTICLE
10.1029/2022JB026332

Characteristics of Slow Slip Events Explained by Rate-Strengthening Faults Subject to Periodic Pore Fluid Pressure Changes

Andrea Perez-Silva[1], Yoshihiro Kaneko[2], Martha Savage[1], Laura Wallace[3,4], and Emily Warren-Smith[3]

[1]School of Geography, Environment and Earth Sciences, Victoria University of Wellington, Wellington, New Zealand, [2]Department of Geophysics, Kyoto University, Kyoto, Japan, [3]GNS Science, Lower Hutt, New Zealand, [4]Institute for Geophysics, University of Texas, Austin, TX, USA

Key Points:

- Periodic pore fluid pressure perturbations on a rate-strengthening fault induce slow slip events (SSEs)
- Source properties of induced SSEs vary with perturbation characteristics (length scale, amplitude, period)
- Model reproduces source properties of shallow Hikurangi SSEs, and duration and magnitude of SSEs in different subduction zones

Supporting Information:

Supporting Information may be found in the online version of this article.

Correspondence to:

A. Perez-Silva,
andrea.perez@vuw.ac.nz

Citation:

Perez-Silva, A., Kaneko, Y., Savage, M., Wallace, L., & Warren-Smith, E. (2023). Characteristics of slow slip events explained by rate-strengthening faults subject to periodic pore fluid pressure changes. *Journal of Geophysical Research: Solid Earth*, *128*, e2022JB026332. https://doi.org/10.1029/2022JB026332

Received 28 DEC 2022
Accepted 30 MAY 2023

Author Contributions:

Conceptualization: Andrea Perez-Silva, Yoshihiro Kaneko, Martha Savage, Laura Wallace, Emily Warren-Smith
Formal analysis: Andrea Perez-Silva, Yoshihiro Kaneko, Emily Warren-Smith
Funding acquisition: Yoshihiro Kaneko, Martha Savage
Investigation: Andrea Perez-Silva, Yoshihiro Kaneko, Martha Savage
Methodology: Andrea Perez-Silva, Yoshihiro Kaneko
Project Administration: Yoshihiro Kaneko, Martha Savage

Abstract Geophysical observations suggest that temporal changes in pore fluid pressure correlate with slow slip events (SSEs) at some subduction zones, including the Hikurangi and Cascadia subduction zones. These fluctuations in pore fluid pressure are attributed to fluid migration before and during SSEs, which may modulate SSE occurrence. To examine the effect of pore fluid pressure changes on SSE generation, we develop numerical models in which periodic pore-pressure perturbations are applied to a stably sliding, rate-strengthening fault. By varying the physical characteristics of the pore-pressure perturbations (amplitude, characteristic length and period), we find models that reproduce shallow Hikurangi SSE properties (duration, magnitude, slip, recurrence) and SSE moments and durations from different subduction zones. The stress drops of modeled SSEs range from ~20–120 kPa while the amplitudes of pore-pressure perturbations are several MPa, broadly consistent with those inferred from observations. Our results indicate that large permeability values of $\sim 10^{-14}$ to 10^{-10} m^2 are needed to reproduce the observed SSE properties. Such high values could be due to transient and localized increases in fault zone permeability in the shear zone where SSEs occur. Our results suggest that SSEs may arise on faults in rate-strengthening frictional conditions subject to pore-pressure perturbations.

Plain Language Summary Slow slip events (SSEs), with slower velocities and longer durations than regular earthquakes, have been detected at several subduction zones worldwide. Recent observations have led researchers to infer that pore fluid pressure—the pressure of fluids in the pore space of rocks—changes during SSEs that occur along the shallow (<15 km depth) portion of the Hikurangi subduction zone, where the Pacific Plate subducts beneath the Australian plate. Similar observations have been reported during SSEs in different subduction zones. However, how pore fluid pressure changes are linked to SSEs is poorly understood. To investigate this issue, we develop physics-based models in which periodic perturbations in pore fluid pressure are imposed on a fault governed by the expected frictional behavior of rocks derived from laboratory experiments. These pore fluid pressure perturbations induce SSEs, and the features of these events (duration, magnitude, peak velocity, recurrence interval) change with the characteristics of the pore fluid pressure change (size, amplitude, and period). After exploring different perturbation characteristics, we find models that capture the observed features of SSEs along the Hikurangi margin and in different subduction zones. This study suggests that pore fluid pressure changes may play an important role in SSE occurrence.

1. Introduction

Indirect geophysical observations, such as variations in seismic velocity, seismic attenuation, seismic anisotropy and principal stresses, have suggested that temporal fluctuations in pore fluid pressure correlate with the occurrence of slow slip events (SSEs) in subduction zones such as Hikurangi (Warren-Smith et al., 2019), Cascadia (Gosselin et al., 2020), Nankai (Kita et al., 2021), and Sagami (Nakajima & Uchida, 2018). Such observations indicate that pore-pressure changes are cyclical, coinciding with SSE recurrence time, which suggests that they play an important role in SSE occurrence. Stress changes interpreted as being related to pore-pressure cycling have been well characterized during SSEs along the shallow (<15 km) portion of the northern Hikurangi margin (offshore Gisborne), where the Pacific plate subducts beneath the Australian plate. Analysis of earthquake focal mechanisms within the subducting Pacific slab during four of these SSEs revealed temporal changes in the relative

Supervision: Yoshihiro Kaneko, Martha Savage
Validation: Andrea Perez-Silva, Laura Wallace, Emily Warren-Smith
Visualization: Andrea Perez-Silva
Writing – original draft: Andrea Perez-Silva
Writing – review & editing: Yoshihiro Kaneko, Martha Savage, Laura Wallace, Emily Warren-Smith

magnitude of the principal stresses, which coincided with the timing of shallow Hikurangi SSEs (Warren-Smith et al., 2019). To explain this, Warren-Smith et al. (2019) suggest that pore pressure within and beneath the fault builds-up during the period prior to an SSE and drops at the onset of SSE slip, as the fluids drain away (bottom inset in Figure 1a).

Pore-pressure cycling during SSEs has been explained through the fault valve model (Gosselin et al., 2020; Warren-Smith et al., 2019). In this model, episodes of fluid accumulation and drainage are driven by the feedback between fault slip, and re-sealing processes, which modulate permeability changes along the plate interface (Sibson, 1990, 1992). Fluids, derived from dehydration reactions within the subducting plate (e.g., Hyndman & Peacock, 2003; van Keken et al., 2011), accumulate within the slab, trapped by the low permeability seal at the plate interface (Audet et al., 2009; Peacock et al., 2011). Continued fluid accumulation builds up overpressure, which eventually breaks the low-permeability seal, inducing slip at the plate interface. The onset of slip opens fractures that act as pathways for fluid migration, which causes a drop in pore fluid pressure (Figure 1a). The cycle continues as mineral precipitation within newly opened fractures re-establishes the low-permeability barrier. Tentative evidence of this process is documented in exhumed subduction zones, where so-called crack-seal veins signal episodes of fracturing and sealing (e.g., Behr & Bürgmann, 2021; Condit & French, 2022). Likewise, variations in isotropic and anisotropic seismic velocity has been attributed to fluid migration through such fractures (Wang et al., 2022; Zal et al., 2020). Notably, the inferred pore-pressure change in these cycles is several MPa (Gosselin et al., 2020; Warren-Smith et al., 2019), while the stress drop of most SSEs ranges from 0.01 to 0.1 MPa (Gao et al., 2012). Such a discrepancy is not intuitive and calls for an explanation.

Within the rate-and-state friction (RSF) framework (Dieterich, 1979), SSEs commonly require rate-weakening friction to nucleate, while different mechanisms (e.g., transition to rate-strengthening friction at higher slip speeds, Shibazaki, 2003; dilatancy strengthening, Segall et al., 2010; transitional friction behavior, Liu & Rice, 2007) have been proposed to stabilize the growing unstable slip. These models, although successful in reproducing SSE characteristics (e.g., Dal Zilio et al., 2020; Li & Liu, 2016; Liu & Rice, 2009; Matsuzawa et al., 2013; Perez-Silva et al., 2021, 2022; Shibazaki et al., 2012, 2019), do not account for the temporal variation in pore pressure nor the widespread occurrence of rate-strengthening materials in slow slip regions (e.g., Bürgmann, 2018; Ikari et al., 2013; Saffer & Wallace, 2015). An alternative modeling approach, proposed by Perfettini and Ampuero (2008), suggests that transient slip is induced in rate-strengthening conditions by external stress perturbations. This approach is consistent with recent numerical models in which changes in pore pressure within rate-strengthening fault zones give rise to aseismic slip (e.g., Dublanchet, 2019; Heimisson et al., 2019; Mallick et al., 2021; Yang & Dunham, 2021).

Recent modeling efforts have focused on the relation between fluids and fault slip to explain different phenomena. In a model that coupled fluid flow, permeability and pore-pressure evolution with RSF, Zhu et al. (2020) found that fluid pressurization induced earthquake swarms and aseismic slip at different parts of the seismogenic zone. In another model, where changes in permeability through fault valving modulated pore-pressure diffusion, Farge et al. (2021) captured realistic tremor-like patterns. Using a different approach, Bernaudin and Gueydan (2018) explained episodic tremor and slip (ETS) characteristics by modeling a brittle-ductile material, governed by microfracturing, sealing and fluid pumping. Other models have also proposed that traveling porosity waves carrying elevated pore-pressure (Skarbek & Rempel, 2016) and pore pressure waves (Cruz-Atienza et al., 2018) may control the periodicity of ETS and the speed of rapid tremor migrations, respectively. All these studies have focused on describing the mechanism whereby pore pressure and fault slip are coupled. However, since they assume either 1-D or 2-D models, direct comparisons to observations have been limited.

In this work, we explore the possibility that periodic pore-pressure perturbations in a rate-strengthening fault zone induce SSEs with source properties (duration, magnitude, peak velocity, recurrence interval, slip) comparable to observations. We consider a relatively simple modeling approach in which fault slip relates to pore-pressure changes through changes in effective stress—the difference between the lithostatic load and pore fluid pressure. This approach is one-way coupled, in that we do not account for the effect of fault slip on fluid flow. Our model targets shallow SSEs in the northern part of the Hikurangi margin (offshore Gisborne), as pore-pressure fluctuations during these events are indicated by seismological observations (Wang et al., 2022; Warren-Smith et al., 2019; Zal et al., 2020). In addition, we investigate whether SSEs in other subduction zones can be explained using the same modeling approach.

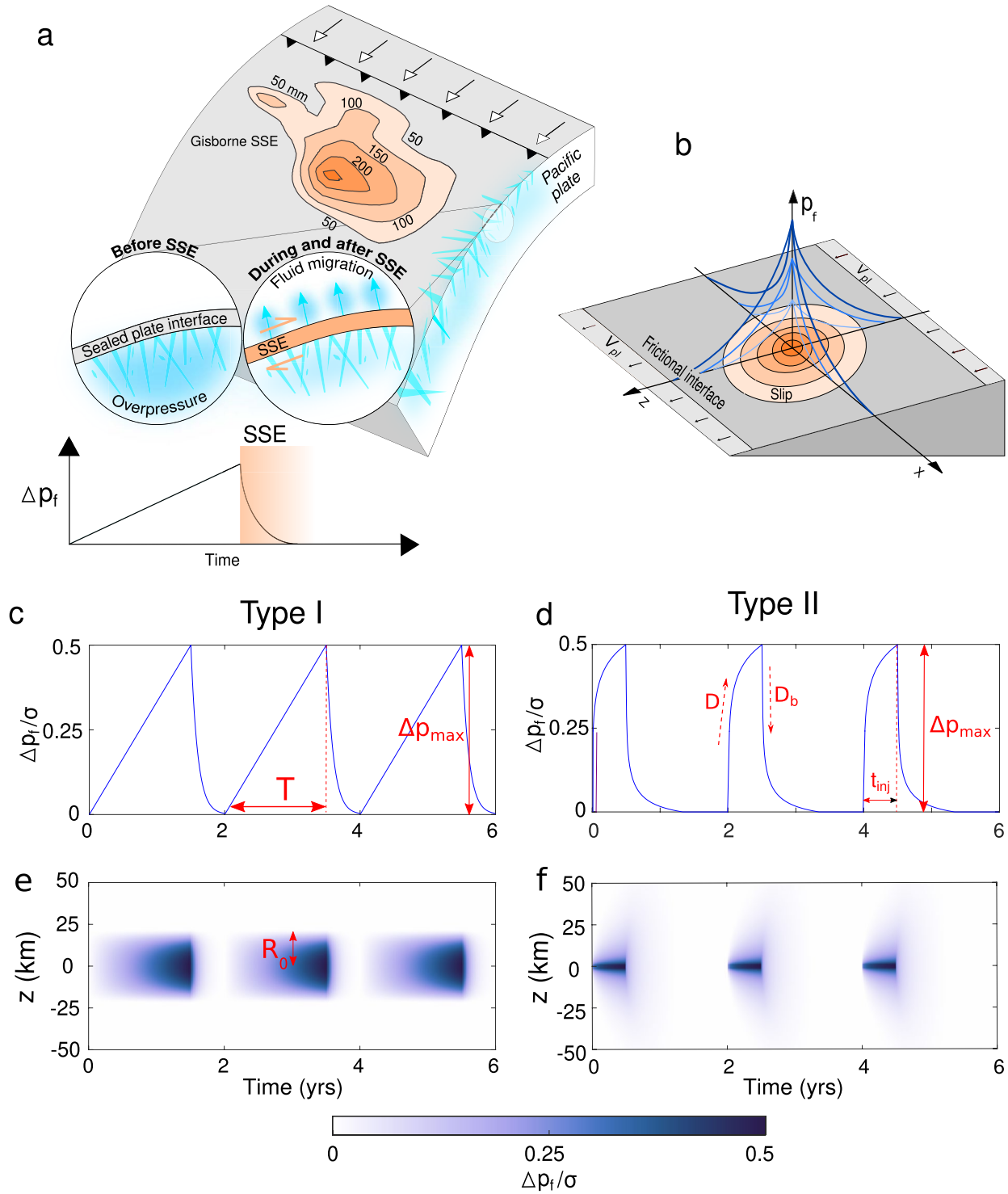

Figure 1. (a) Schematic diagram representing a conceptual model of pore-pressure cycling during shallow Hikurangi slow slip event (SSE), based on Warren-Smith et al. (2019). Orange contours show cumulative slip during 2016 shallow Gisborne SSE (Wallace et al., 2016). Thick blue lines indicate fractures. The bottom inset shows the inferred change in pore fluid pressure within the subducting Pacific slab during an SSE (modified from Figure 4a in Warren-Smith et al. (2019)). (b) Schematic of our model setup showing pore-pressure increase at the fault center (blue lines; different shades indicate different time steps) and ensuing slip (orange contours) on the plate interface. Note that this schematic representation is more consistent with type II perturbation (Section 2.3.2) than with type I perturbation (Section 2.3.1). (c–f) Examples of modeled pore fluid pressure changes for (c, e) type I and (d, f) type II perturbations. Temporal change in pore fluid pressure is shown (c, d) at the fault center and (e, f) along z. Perturbation parameters shown are explained in Section 2.3.

Table 1
Model Parameters Used in This Study

Parameter	Symbol	Value
Characteristic slip distance	D_{RS}	5 mm
Direct effect	a	0.005
Evolution effect	b	0.004
Background effective normal stress	σ	3 MPa (9 MPa)[a]
Shear modulus	μ	10 GPa (30 GPa)[a]
Characteristic size of process zone	$L_b = \mu D_{RS}/b\sigma$	4.17 km
Reference friction coefficient	f_0	0.6
Reference slip velocity	V_0	10^{-6} m/s
Poisson's ratio	ν	0.25
Loading rate	V_{pl}	50 mm/yr[b]
Spatial resolution	Δx	0.39–0.78 km

[a]σ and μ used in simulation cases shown in Section 5, except for modeled shallow Hikurangi SSEs. [b]Different V_{pl} were considered in Figure 10, see Table 4.

2. Model Setup

2.1. Fault Model

Our modeling approach is built upon the one developed by Lapusta and Liu (2009), which was adapted to model slip on subduction faults by Kaneko et al. (2010). Our model consists of a planar fault embedded in an infinite elastic medium. The fault is loaded by a long-term plate rate at the upper and lower ends along depth (z). Fault slip is governed by the balance between the shear stress on the fault, given by the elastodynamic relation (Text S1 in Supporting Information S1), and the frictional strength τ, given by the following equation:

$$\tau(x, z; t) = f[\sigma - \Delta p_f(x, z; t)], \quad (1)$$

where f is the friction coefficient, σ is the background normal stress and Δp_f is the pore fluid pressure change. Pore-pressure perturbations are imposed by varying the effective normal stress ($\sigma - \Delta p_f$), where σ is constant and Δp_f evolves in time and space (Section 2.3). We assume pore-pressure changes and fault slip are related via changes in effective normal stress (i.e., one-way coupling).

The evolution of the friction coefficient f is governed by the laboratory-derived rate-and-state friction laws (Dieterich, 1979; Ruina, 1983), that describe f as a logarithmic function of the slip rate V and a state variable θ:

$$f = f_0 + a\ln(V/V_0) + b\ln(V_0\theta/D_{RS}), \quad (2)$$

where f_0 is the steady state friction coefficient at reference rate V_0, D_{RS} is the characteristic slip for state evolution, V is the slip rate, and a and b are the direct and evolution effect, respectively. To describe the evolution of the state variable, we adopt the aging law (Dieterich, 1979; Marone, 1998):

$$\frac{d\theta}{dt} = 1 - \frac{V\theta}{D_{RS}}. \quad (3)$$

2.2. Fault Model Parameters

Model parameters are given in Table 1. The fault is loaded by a uniform, along-dip plate rate (V_{pl}) of 50 mm/yr, consistent with the estimated convergence rate offshore Gisborne, in the northern Hikurangi margin (Wallace et al., 2004). To account for the shallow depths of Gisborne SSEs, we set the shear modulus (μ) to 10 GPa, which is within the range (6–14 GPa) inferred at the central Hikurangi margin using full-waveform inversion of controlled-source seismic data (Arnulf et al., 2021). The Poisson's ratio is set to 0.25, corresponding to a Poisson solid.

We consider uniform friction properties on the fault, where $a = 0.005$ and $b = 0.004$ ($a/b = 1.25$). These values are within the range (10^{-4} to 10^{-2}) obtained in friction experiments on incoming sediments to the Hikurangi margin (e.g., Boulton et al., 2019; Eijsink & Ikari, 2022; Ikari et al., 2020). Such experiments show that frictional stability trends span rate-strengthening, rate-neutral, and rate-weakening behaviors. In this study, we focus exclusively on rate-strengthening friction. Unstable slip under rate-strengthening conditions can initiate due to external stress perturbations (Perfettini & Ampuero, 2008). In our model, the increase in pore pressure reduces fault strength, thus promoting slip.

The spatial discretization must resolve the characteristic size of the process zone $L_b = \mu D_{RS}/b\sigma$ (Ampuero & Rubin, 2008; Perfettini & Ampuero, 2008), which is 4.17 km for all simulations presented. The grid spacing Δx is chosen as a fraction of L_b, typically $\Delta x = L_b/5$. Each simulation takes from 20 min up to 4 hr on 64 physical cores of the New Zealand eScience Infrastructure's Cray XC50 computer. To save computational costs, we set $\sigma = 3$ MPa, which is below the estimated range (10–30 MPa) along the shallow Hikurangi margin (Arnulf et al., 2021). We could scale up σ by reducing the constitutive parameters a and b so that $a\sigma$ and $b\sigma$ remain constant, and obtain the same results, as expected from Equations 1 and 2 (e.g., Perez-Silva et al., 2022).

2.3. Models of Pore-Pressure Cycling

To model the inferred pore-pressure cycling, we impose periodic perturbations in pore pressure on a rate-strengthening planar fault, as schematically shown in Figure 1b. We define two types of perturbations to describe the evolution of pore pressure in space and time. While both perturbations consider a one-way coupling between fault slip and pore-pressure (Section 2.1), they differ in the temporal and spatial evolution of pore pressure, as explained in the following. We assume that the period of the pore-pressure cycles is the same as the recurrence interval of shallow Gisborne SSEs, as proposed by Warren-Smith et al. (2019). Note that we do not model the mechanism that controls the period of the pore-pressure cycle.

2.3.1. Type I Perturbation: Sawtooth-Like Pore-Pressure Changes

Within the subducting slab, temporal pore-pressure changes were proposed to follow a 'sawtooth' pattern during shallow Hikurangi SSEs (bottom inset in Figure 1a, Warren-Smith et al., 2019). Following that concept, we define the temporal evolution of pore pressure as shown in Figure 1c. For simplicity, the spatial pore-pressure change is defined as a Gaussian distribution (Figure 1e). Even though we do not model the mechanism whereby fluid migrates, we envision that it is normal to the fault and that there is no along-fault fluid migration.

The evolution of pore pressure in space and time is given by:

$$\Delta p_f(r,t^*) = \Delta p_{max}\exp\left(\frac{r^2}{r^2-R_0^2}\right)\left[\frac{t^*}{T}H(T-t^*)+e^{-C(t^*-T)}H(t^*-T)\right] \text{ for } r < R_0, \quad (4)$$

where Δp_f is the pore-pressure change in MPa, r is the radial distance from the fault center in km, t^* is the time since the start of the perturbation in yr, Δp_{max} is the maximum pore-pressure change in MPa, R_0 is the perturbation radius in km and T its duration in yr. C represents the exponential decay rate of pore pressure, which we set to 10 yr^{-1} to model the inferred rapid decrease in Δp_f (bottom inset in Figure 1a). $H(t)$ is the Heaviside function; $H(t) = 0$ for $t < 0$ or $H(t) = 1$ for $t > 0$. Equation 4 shows that the size and amplitude of perturbations are controlled by R_0 and Δp_{max}. Following Perfettini and Ampuero (2008), we express them in terms of non-dimensional parameters R_0/L_b and $\Delta p_{max}/a\sigma$, respectively.

2.3.2. Type II Perturbation: Along-Fault Fluid Diffusion

The second type of perturbation is motivated by fluid injection experiments (Cappa et al., 2019; Guglielmi et al., 2015) and numerical models (Dublanchet, 2019; Larochelle et al., 2021; Yang & Dunham, 2021; Zhu et al., 2020), in which aseismic slip is induced by the injection of fluids that diffuse into the fault zone. In this perturbation, fluid flow is driven by diffusion along the fault plane, while there is no flow in the fault-normal direction. We prescribe that fluids are injected into the fault plane from the wall of a circular cylinder of radius r_0, perpendicular to the fault plane. Fluid flow occurs only within the fault plane and is fault-parallel and axisymmetric with respect to the axis of the circular cylinder (Sáez et al., 2022). Fluid is injected at a constant rate q_0 (in m/s) and diffuses along the fault plane following the axisymmetric fluid diffusion equation:

$$\frac{\partial p_f(r,t)}{\partial t} = D\left(\frac{\partial^2 p_f(r,t)}{\partial r^2}+\frac{1}{r}\frac{\partial p_f(r,t)}{\partial r}\right), \quad (5)$$

where r is the radial distance in km and D is the hydraulic diffusivity in m^2/s, which we assume is uniform on the fault plane. For simplicity, our model does not account for permeability and porosity evolution, which may also affect the fault response (Yang & Dunham, 2021; Zhu et al., 2020). In the time domain, the solution of Equation 5 can be expressed in the following functional form (eq. 7.647, Cheng, 2016):

$$p_f(r,t) = \frac{q_0 r_0}{\kappa}\,\Pi(r,t), \quad (6)$$

where κ is the permeability or mobility coefficient (i.e., permeability to dynamic viscosity ratio) in $m^2/Pa{\cdot}s$ and Π is the dimensionless pore-pressure evolution, given by (Section 13.5, eq. 17, Carslaw & Jaeger, 1959):

$$\Pi(r,t) = -\frac{2}{\pi r_0}\int_0^\infty \left(1-e^{-Du^2 t}\right)\frac{J_0(ur)Y_1(ur_0)-Y_0(ur)J_1(ur_0)}{u^2\left[J_1^2(ur_0)+Y_1^2(ur_0)\right]}du, \quad (7)$$

where J_i and Y_i are respectively the Bessel function of the first and second kind of order i, where $i = 0$ or 1. Note that the factor $1/r_0$ in Equation 7 is included in the errata of eq. 7.647 in Cheng (2016). To model the pore-pressure perturbation, we use the exact solution of Equation 7 solved via numerical inversion of the Laplace transform (Cheng, 2016; Stehfest, 1970). We note that Equation 7 is valid for $r \geq r_0$.

The evolution of pore-pressure during the perturbation is given by:

$$\Delta p_f(r, t^*) = \frac{q_0 r_0}{\kappa}\left[\Pi(r, Dt^*)H(t^*) - \Pi\left(r, D_b\left(t^* - t_{inj}\right)\right)H\left(t^* - t_{inj}\right)\right], \tag{8}$$

where t_{inj} is the time over which fluids flow into the fault plane, and D and D_b are the hydraulic diffusivity before t_{inj} and after t_{inj}, respectively. Equation 8 shows that fluids diffuse from the cylinder wall along the fault plane over time t_{inj}, thus increasing pore pressure. After t_{inj}, pore-pressure decreases as fluids diffuse away from the fault with diffusivity D_b (Figures 1d and 1f). We consider $D_b > D$ to model the rapid drop in pore pressure inferred by observations (see bottom inset in Figure 1a).

Similar to type I case, the perturbation characteristics are its size and amplitude. The size of the perturbation is controlled by the diffusion length $\sqrt{Dt_{inj}}$, which represents the evolution of the pore-pressure front, while the maximum pore-pressure change Δp_{max} determines its amplitude. We define D, t_{inj} and Δp_{max} as input parameters. To obtain a given Δp_{max}, we solve for q_0/κ using Equation 8. The normalized perturbation size and amplitude correspond to $\sqrt{Dt_{inj}}/L_b$ and $\Delta p_{max}/a\sigma$, respectively. We note that the characteristic length scale of the diffusion process is $\sqrt{Dt_{inj}}/r_0$. However, to account for the effect of the fault properties, we consider L_b instead of r_0 in the characteristic length of the perturbation ($\sqrt{Dt_{inj}}/L_b$), consistent with type I case (R_0/L_b). The length scale r_0 could be interpreted as the width of the fluid source. Unless otherwise noted, we assume $r_0 = 1$ km to ensure that r_0 is properly resolved by our simulations ($\Delta x \leq 0.78$ km, Table 1). In Section 5.1, we discuss the implications of different r_0. Note that, since Equation 7 is valid for $r \geq r_0$, we simply assume a constant value $\Delta p_f(r_0, t^*)$ within $0 < r < r_0$.

2.4. Quantification of Source Properties of Induced SSEs

To report the source properties of SSEs induced by pore-pressure perturbations, we first define a velocity threshold (V_{thr}). SSE duration corresponds to the time over which the maximum slip rate on the fault exceeds V_{thr}. We calculate the corresponding SSE moment using the SSE area and the slip accumulated over the SSE duration. To calculate the accrued slip, we consider the slip over the cells with slip larger than a minimum slip, defined as $1.1 \times V_{pl} \times$ SSE duration. This definition ensures that the accumulated slip exceeds the slip accrued due to a given plate loading rate over the SSE duration.

To calculate the stress drop of induced SSEs, we use the energy-based approach by Noda et al. (2013). In this approach, the stress drop $\overline{\Delta\sigma}_E$ is calculated by averaging the stress change distribution with the final slip at each cell as the weighting function (Noda et al., 2013):

$$\overline{\Delta\sigma}_E = \frac{\int_\Sigma \Delta\sigma\, \Delta u\, dS}{\int_\Sigma \Delta u\, dS} \tag{9}$$

where Σ is the SSE source area, which corresponds to the region with slip greater than the minimum slip defined above, Δu is the final slip distribution of the SSE, and $\Delta\sigma$ is the difference between the shear stress distribution at the start of the SSE and at the end of the SSE. Δu and $\Delta\sigma$ depend on SSE duration and thus on V_{thr}.

The value of V_{thr} depends on the resolution of the instrumentation used to detect SSEs. In the case of shallow Hikurangi SSEs, as they occur offshore, GPS resolution is lower (~2 mm/day) than in other margins where SSEs occur beneath GPS networks (e.g., ~ 0.25– 0.5 mm/day, Wech & Bartlow, 2014). To compare our model results with observed SSE properties at Hikurangi, we set $V_{thr} = 2$ mm/day. We set a lower threshold of $V_{thr} = 0.3$ mm/day to estimate the sensitivity of SSE source properties to the perturbation characteristics. Unless otherwise noted, $V_{thr} = 0.3$ mm/day.

3. Fault Response to Periodic Pore-Pressure Perturbations

Periodic pore-pressure perturbations of type I and II can induce SSEs, whose recurrence interval is controlled by the period of the perturbation. We explore the controlling parameters of each perturbation type (size: R_0/L_b

Table 2
Perturbation Characteristics for Representative Models of Shallow Gisborne Slow Slip Events (SSEs) Under Type I and Type II Perturbations (Section 3)

	Perturbation parameters	Symbol	Value in representative model
Type I	Duration of pressurization phase	T	1.5 yr
	Radius	R_0	33.75 km
	Maximum amplitude	Δp_{max}	1.88 MPa
	Normalized length-scale	R_0/L_b	~8
	Normalized amplitude	$\Delta p_{max}/a\sigma$	125
Type II	Fluid "injection" time	t_{inj}	30 days
	Hydraulic diffusivity (pressurization)	D	25 m^2/s
	Hydraulic diffusivity (depressurization)	D_b	40 m^2/s
	Cylinder radius	r_0	1 km
	Maximum amplitude	Δp_{max}	1.5 MPa
	Normalized length scale	$\sqrt{Dt_{ini}}/L_b$	1.93
	Normalized amplitude	$\Delta p_{max}/a\sigma$	100

Note. Perturbation period is 2 yr for both cases.

or $\sqrt{Dt_{inj}}/L_b$, and amplitude: $\Delta p_{max}/a\sigma$) and their effect on induced SSE properties in Section 4. Based on the parameter exploration, we find two representative models (one for each perturbation type) that induce SSEs with properties comparable to those of shallow Gisborne SSEs, which have durations of 6–34 days, M_w6.2 − 6.5, maximum slip of 4–27 cm and recurrence of ~2 yr (Ikari et al., 2020). The perturbation characteristics for each representative model are given in Table 2, and Table 3 compares modeled and observed Gisborne SSE properties. Note that the representative models are non-unique, as different parameter combinations lead to SSEs with source properties comparable to the observed range. In the following, we describe the fault response for these two models. We note that conditions at the start of the simulations ($t = 0$) and first perturbation ($t = 20$ yr) are at or very close to steady state (Table S1 in Supporting Information S1).

3.1. Representative Model for Type I Perturbation

At $t = 20$ yr, we impose a pore-pressure perturbation every 2 yr (red line in Figure 2a) with $R_0 = 33.8$ km and $\Delta p_{max} = 1.88$ MPa (Table 2). This perturbation induces SSEs characterized by the increase in the maximum slip velocity on the fault (V_{max}, blue line in Figure 2a). After the first few pore-pressure cycles, the fault response is the same after each perturbation, with V_{max} rising ~3 orders of magnitude above the plate rate (Figure 2a).

To illustrate the fault response during the periodic pore-pressure perturbations, we show the evolution of different field variables (V/V_{pl}, θ, $\sigma - \Delta p_f$, τ and f) at $(x, z) = (0, 5$ km) in Figure 2b. At the start of the perturbations, the decrease in the effective normal stress ($\sigma - \Delta p_f$, green dashed line in Figure 2b), due to the rising pore pressure,

Table 3
Range of Source Properties of Observed Slow Slip Events (SSEs) Offshore Gisborne (Taken From Ikari et al. (2020)'s Catalog) Compared With Average Properties of Modeled SSEs From Two Representative Models for Type I and Type II Perturbation (Section 3)

Source property	Observed SSEs offshore Gisborne	Model type I	Model type II
Duration (days)	6 − 34	25.6 ± 0.03	26.7 ± 0.03
Magnitude (M_w)	6.2 − 6.5	6.2	6.1
Maximum slip (cm)	4 − 27	10.0 ± 0.01	9.98 ± 0.03
Recurrence interval (yrs)	~2	2	2

Note. To calculate SSE properties we set a velocity threshold (V_{thr}) of 2 mm/day, consistent with the resolution limit of GPS network for shallow Hikurangi SSEs (Section 2.4).

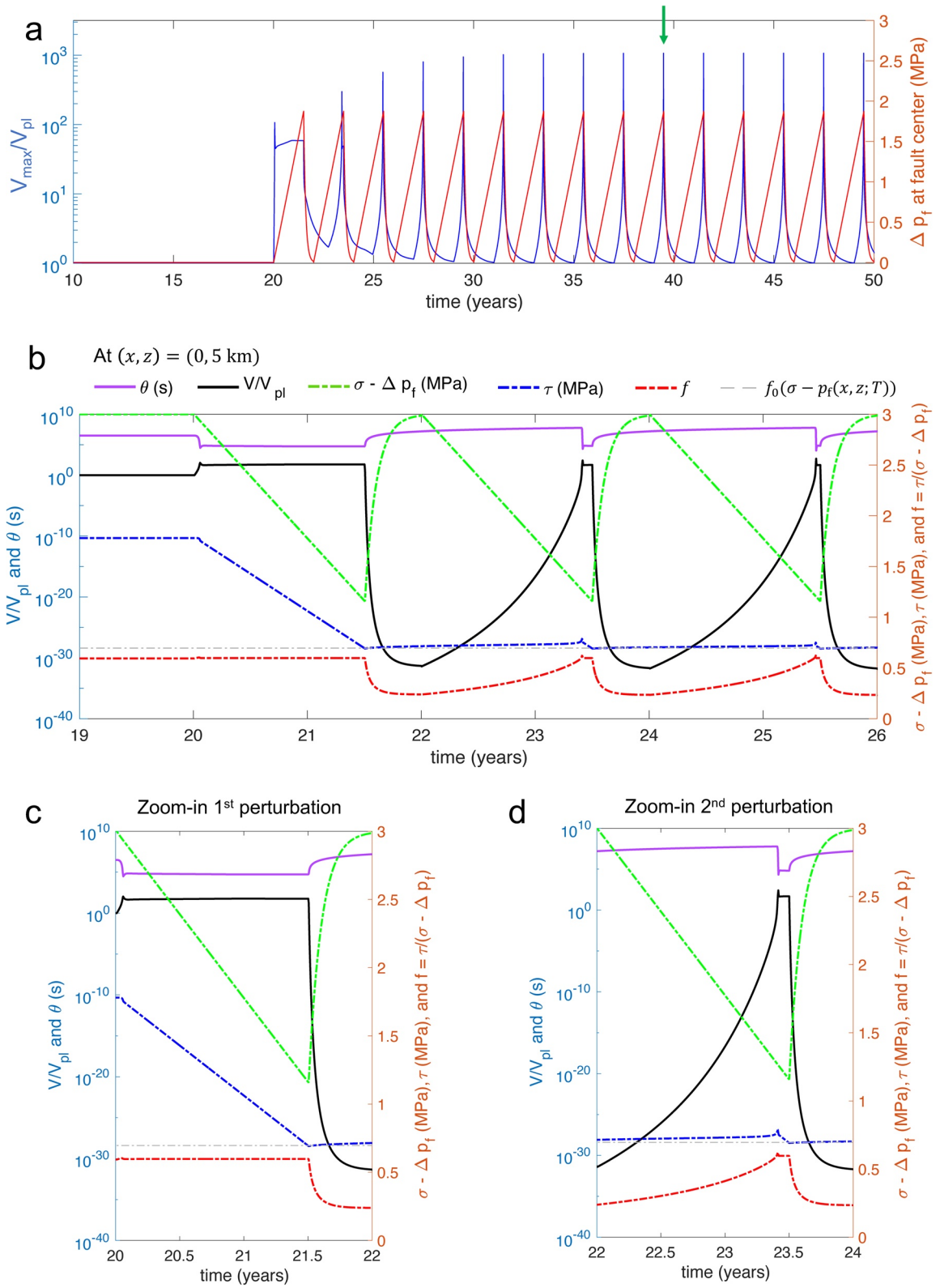

Figure 2. Fault response for representative model under type I perturbation. (a) Temporal evolution of (blue line) the maximum slip rate on the fault normalized with respect to the plate rate (V_{max}/V_{pl}) and (red line) the pore pressure evolution Δp_f at the fault center. Green arrow indicates the slow slip event (SSE) shown in Figures 3a–3f and Figure S1 in Supporting Information S1. (b) Temporal evolution of field variables at (x, z) = (0, 5 km). State variable (θ in s, purple line), normalized slip rate (V/V_{pl}, black line), effective normal stress ($\sigma - \Delta p_f$ in MPa, green dashed line), shear stress (τ in MPa, dashed blue line), friction coefficient (f, dashed red line). The value of $f_0(\sigma - p_f(x, z; T))$, where ($x$, z) = (0, 5 km) and T = 1.5 yr, is shown by the gray dashed line. Zoom-in during (c) first and (d) second perturbations.

is accompanied by an increase in the slip velocity (V/V_{pl}, black line in Figure 2b) and a change in shear stress (τ, dashed blue line in Figure 2b), which decreases in proportion to the effective stress decrease. Notably, at the end of the pressurization phase ($t = 21.5$ yr), the shear stress is equivalent to $f_0(\sigma - \Delta p_f(x, z; T))$, where $(x, z) = (0, 5$ km) and $T = 1.5$ yr (dashed gray line in Figure 2b). Following Equation 1, the fault response shows that, to the first order, the pore pressure increase at the start of the perturbations is compensated by a reduction in the shear stress. During depressurization (21.5 yr $< t <$ 22 yr), the slip velocities drastically drop far below V_{pl} ($V/V_{pl} \sim 10^{-30}$), and the friction coefficient decreases to $f \sim 0.2$ (dashed red line in Figure 2b) at the end of the perturbation ($t = 22$ yr). Conditions at the onset of the second perturbation are markedly different from those at the first perturbation (cf. Figures 2c and 2d), as the fault is below steady state with $\tau \sim f_0(\sigma - \Delta p_f(x, z; T))$ and $V \ll V_{pl}$ (Figure 2d and Table S1 in Supporting Information S1). During the second perturbation, the shear stress remains approximately constant during the pressurization phase (22 yr $< t <$ 23 yr) and changes when slip rates become significant, $V > 10\ V_{pl}$, which occurs close to the end of this phase ($t \sim 23.5$ yr in Figure 2d). In this case, the decrease in shear stress is much lower than for the first perturbation (cf. dashed blue lines in Figures 2c and 2d). During the second perturbation, the pore-pressure increase is compensated by an increase in f via rising slip rates (Equation 1). Depressurization for the second perturbation has the same characteristics as for the first. For subsequent perturbations, the fault response is essentially the same as for the second perturbation and is characteristic after the 5th perturbation (Figure 2a).

To visualize the fault response during an induced SSE, we show snapshots of the slip velocity in Figures 3a–3f (see also Movie S1 and Figure S1 in Supporting Information S1) and contours of the pore-pressure change ($\Delta p_f/\sigma$, solid lines). We show the 10th induced SSE in the sequence (green arrow in Figure 2a), as the fault response is the same after each perturbation from the 5th induced SSE. The slip rate evolution can be divided into four consecutive phases: (a) During the last stages of pore-pressure increase ($t^* > 1$ yr), the slip rate accelerates from the edges of the perturbation and propagates toward the center of the fault (Figures 3a and 3b). Meanwhile, the central fault patch, which starts off fully locked (Figure 3a), gradually unlocks as it shrinks down (Figure 3b). In this phase, the friction coefficient increases by raising slip rates to compensate for the decrease in effective normal stress (Equation 1). (b) Slip fronts coalesce at the fault center, where the slip rate is maximum (Figure 3c). (c) Slip rate decelerates as slip fronts migrate away from the center (Figure 3d). Most of the slip accumulates during phases a to c (Figure S2 in Supporting Information S1). (d) At the onset of depressurization, the slip velocity rapidly drops within the pressurized area (Figure 3e). In this case, the drop in slip rate balances the increasing effective normal stress, a response opposite to that in phase (a). At the end of the perturbation, the pressurized area is fully locked (Figure 3f) with $V/V_{pl} \sim 10^{-30}$ (Figure 2b and Figure S1 in Supporting Information S1). While these velocities are below the range of slip rates applicable to RSF, there are no observational constraints to distinguish velocities below $\sim 10^{-11}$ m/s.

To characterize further the induced SSE, we show the shear stress change after this event in Figure 4a. Notably, the stress change within the perturbed area is in the order of kPa. Based on the distribution of shear stress change, we calculate the stress drop $\overline{\Delta\sigma_E}$, as described in Section 2.4. For this event, $\overline{\Delta\sigma_E} = 11.3$ kPa. Thus, the stress drop is much lower than the imposed pore-pressure change, which is in the order of MPa (Table 2). This difference is expected from Figure 2b since the first perturbation induces a change in the distribution of the shear stress on the fault, which drops in proportion to the pore pressure increase and does not recover its value before the start of the perturbations (at $t <$ 20 yr, when $\tau = f_0\sigma$). We note that the stress drop of the first induced SSE is in the order of MPa since it starts from a higher pre-stress level (Figure 2c).

3.2. Representative Model for Type II Perturbation

We apply a pore-pressure perturbation every 2 yr (red line in Figure 5a) with $\sqrt{Dt_{inj}} \sim 8$ km and $\Delta p_{max} = 1.5$ MPa (Table 2). Similar to the previous model, V_{max} (blue line in Figure 5a) transiently increases in response to the perturbations, signaling SSEs. After the first few cycles, the fault response is characteristic and SSEs with $V_{max} \sim 10^{2.4} V_{pl}$ are induced after each perturbation (Figure 5a).

The evolution of slip rates and shear stresses in response to type II perturbation is comparable to that in type I case (Figure 5b). The main difference is that the slip rate and shear stress evolve over a shorter time for type II case, which is due to the short pressurization phase ($t_{inj} = 30$ days). The effective stress decrease at $(x, z) = (0, 5$ km) is much lower than for type I case (cf. dashed green line in Figures 2b and 5b), due to the different shape of the perturbation. The slip rate (black line in Figure 5b) rapidly increases during pressurization and drops during depressurization, alongside the friction coefficient (dashed red line in Figure 5b). On the other hand, the shear

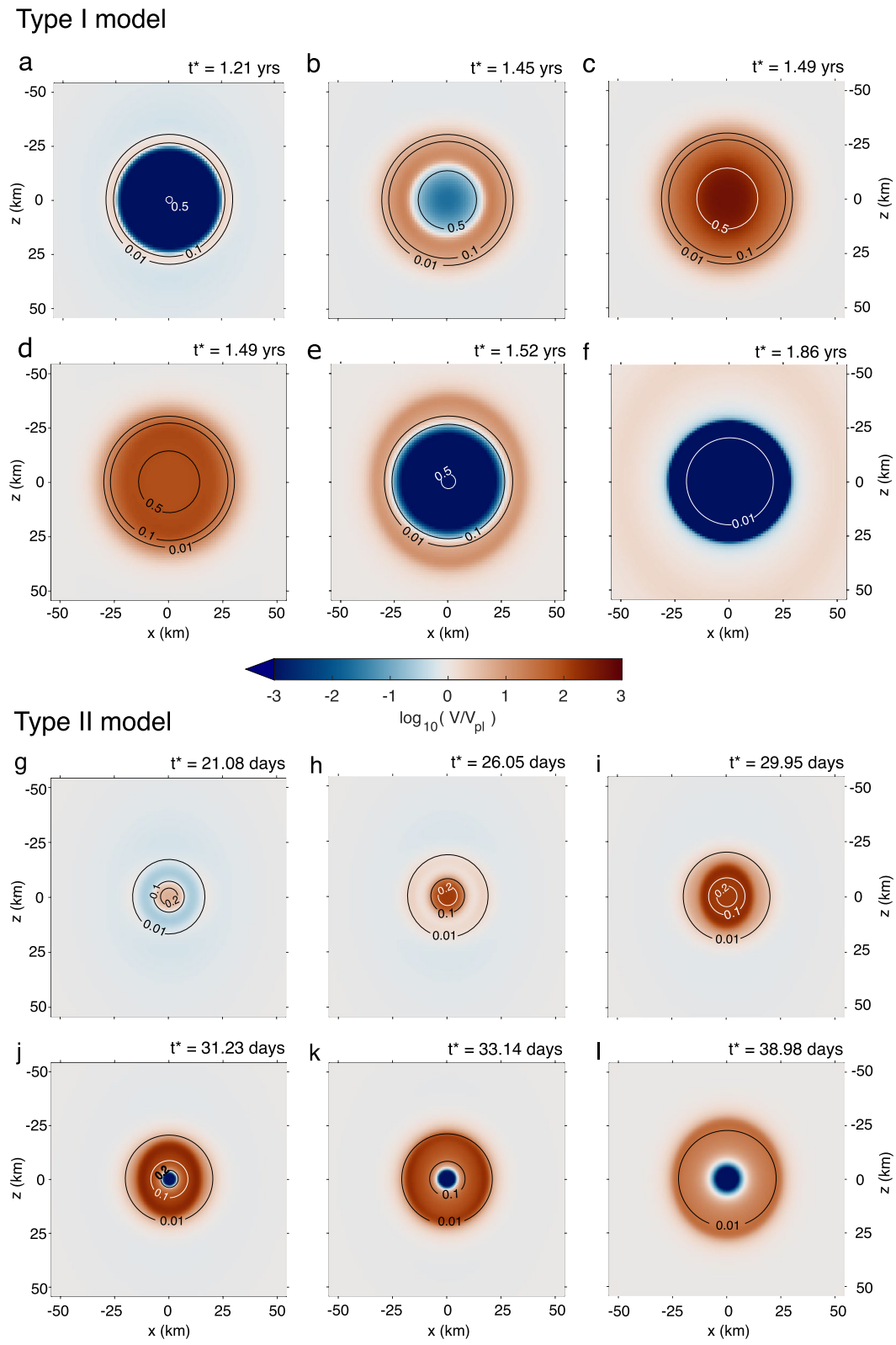

Figure 3. Snapshots of slip rate on the fault during an induced SSE for representative model under (a–f) type I and (g–l) type II perturbations. Slip rate evolution during pore-pressure increase shown in (a–d) and (g–i), and pore-pressure decrease shown in (e–f) and (j–l). Solid lines indicate the contours of the normalized iso-pressure change, $\Delta p_f/\sigma$. t^* shows the time since the start of the perturbation.

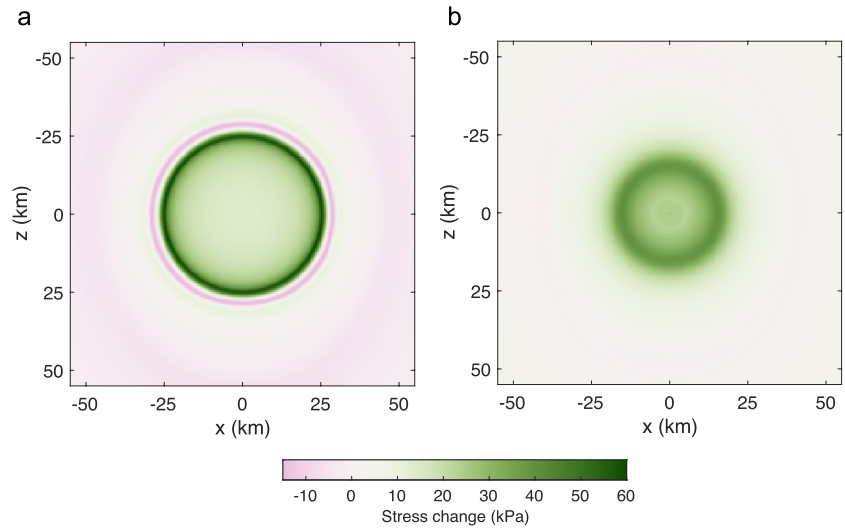

Figure 4. Shear stress change during induced slow slip events (SSEs) shown in Figure 3 for representative models under (a) type I and (b) type II perturbations. The shear stress change is defined as the difference between the shear stress before and after the SSE.

stress (dashed blue line in Figure 5b) decreases at the start of the perturbations ($t > 20$ yr) and remains close to that value in the period between perturbations (20.2 yr $< t <$ 22 yr). The change in shear stress for the second perturbation is much lower, in the order of kPa, and occurs as the slip rate accelerates ($V/V_{pl} \sim 10$), close to the end of pressurization ($t \sim 22.1$ yr in Figure 5d), which is similar to the behavior in type I case. Conditions at the onset of the second perturbation are also different from those of the first (cf. Figures 5c and 5d, and Table S1 in Supporting Information S1). We note that the fault response during SSEs is the same after the first few perturbation cycles.

The slip rate evolution on the fault during an induced SSE (green arrow in Figure 5a) is illustrated in Figures 3g–3l, where pore-pressure contours ($\Delta p_f/\sigma$, solid lines) are also drawn (see also Movie S2 in Supporting Information S1). We can again divide the fault response into four consecutive phases. (a) Slip acceleration localizes at the center of the fault, where the slip rate is maximum (Figure 3g). In this phase, the slip rate increases to balance the decrease in effective stress. (b) Slip acceleration transitions into crack expansion (Figures 3h and 3i), and the maximum slip rate localizes at the crack tip. During this phase, the slow-slip front migrates faster than the pore-pressure front; as seen in previous models of fluid-driven aseismic slip (Bhattacharya & Viesca, 2019; Dublanchet, 2019). (c) As pore-pressure decreases, starting from the injection point, two competing effects take place. Around the injection point, slip rate decelerates below V_{pl}, whereas away from the injection point, crack expansion continues (Figures 3j and 3k). (d) Ongoing depressurization causes deceleration, as the slip rate decreases across the fault, with the central fault patch locked (Figure 3l). Just as for type I case, during depressurization, the slip rate decreases to balance the increasing effective stress (Equation 1).

To explain the evolution of the fault response during the induced SSE, we show the along-depth profiles of $\Delta p_f/\sigma$, V/V_{pl}, $f = \tau/(\sigma - \Delta p_f)$ and Ω (Figure 6). $\Omega = V\theta/D_{RS}$ measures the proximity to steady state, where $\Omega = 1$ is at steady state, $\Omega > 1$ is above steady state and $\Omega < 1$ is below steady state (Rubin & Ampuero, 2005). The fault is below steady state at the onset of pressurization ($\Omega < 1$ for $t^* < 10$ days in Figure 6d), as expected from Figure 5b since $V \ll V_{pl}$. During this initial phase, slip rates increase, although V remains below V_{pl} (Figure 6b). Significant slip rates (phase a) arise close to the end of pressurization ($t^* > 20$ days, Figure 6b), which is when most of the slip accumulates (Figure S2 in Supporting Information S1). This phase is correlated with increasing f (Figure 6c) and Ω (Figure 6d). During crack expansion (phase b), the fault is at or close to steady state within the expanding crack ($\Omega \sim 1$ for $t^* > 25$ days, Figure 6d). The friction coefficient at steady state (or residual friction) is ~0.60 within the crack, while the peak friction is reached at the crack tip, where $f \sim 0.62$ (Figure 6c). During depressurization (phases c and d), V/V_{pl} and f decrease starting from the injection point (Figures 6f and 6g, respectively), where the fault is below steady state ($\Omega \ll 1$, Figure 6h).

Similar to the previous model, the shear stress change after the induced SSE is in the order of kPa (Figure 4b) while the stress drop is 12.3 kPa, which is comparable to the value in type I case ($\overline{\Delta\sigma_E} = 11.3$ kPa). The stress

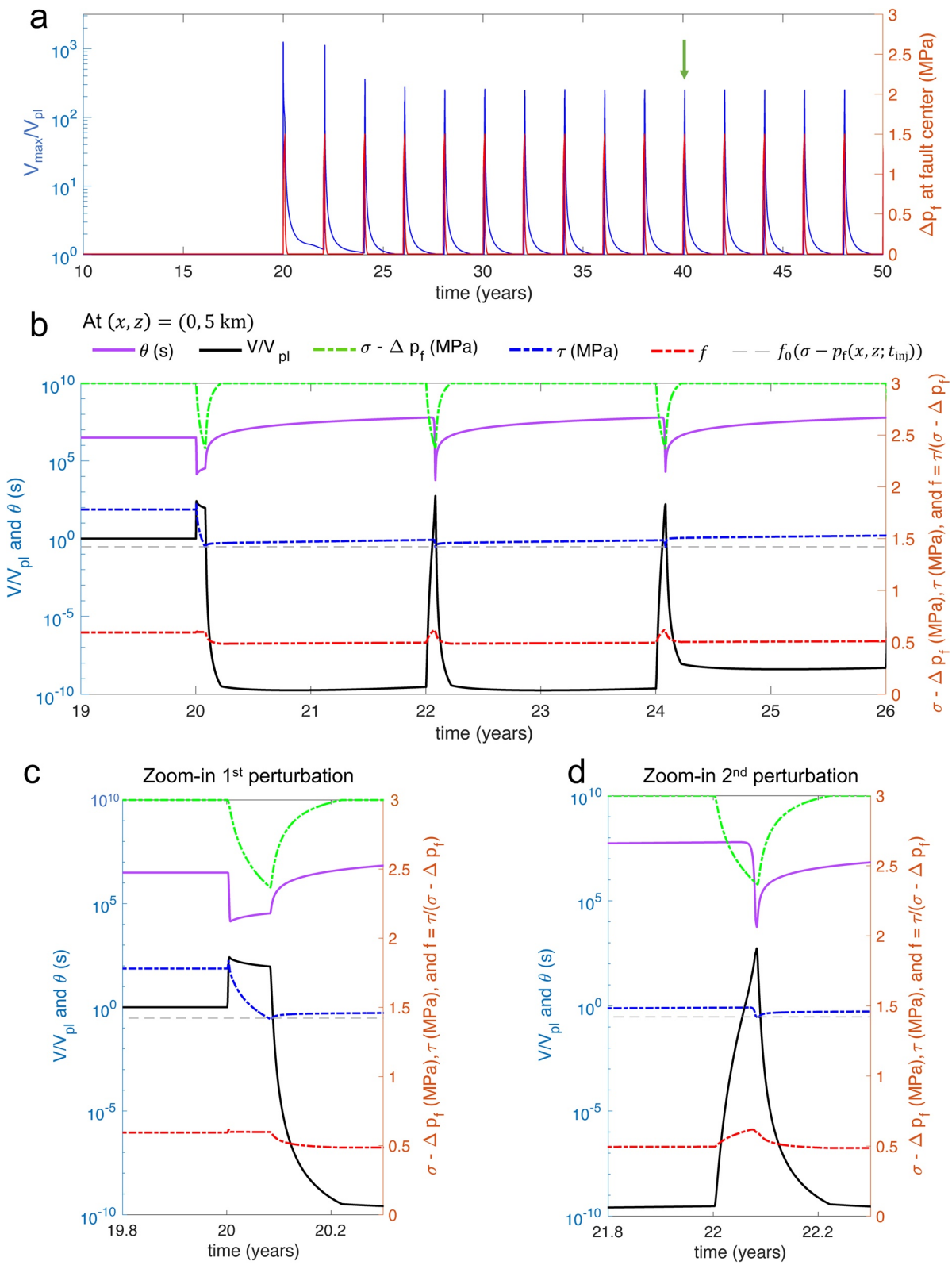

Figure 5. Fault response for representative model under type II perturbation. (a) Temporal evolution of (blue line) the maximum slip rate on the fault normalized with respect to the plate rate (V_{max}/V_{pl}) and (red line) the pore pressure evolution Δp_f at the fault center. Green arrow indicates the slow slip event (SSE) shown in Figures 3g–3l and Figure 6. (b) Temporal evolution of field variables at $(x, z) = (0, 5$ km). State variable (θ in s, purple line), normalized slip rate (V/V_{pl}, black line), effective normal stress ($\sigma - \Delta p_f$ in MPa, green dashed line), shear stress (τ in MPa, dashed blue line), friction coefficient (f, dashed red line). The value of $f_0(\sigma - \Delta p_f$ $(x, z; t_{inj}))$, where $(x, z) = (0, 5$ km) and $t_{inj} = 30$ days, is shown by the gray dashed line. Zoom-in during (c) first and (d) second perturbations.

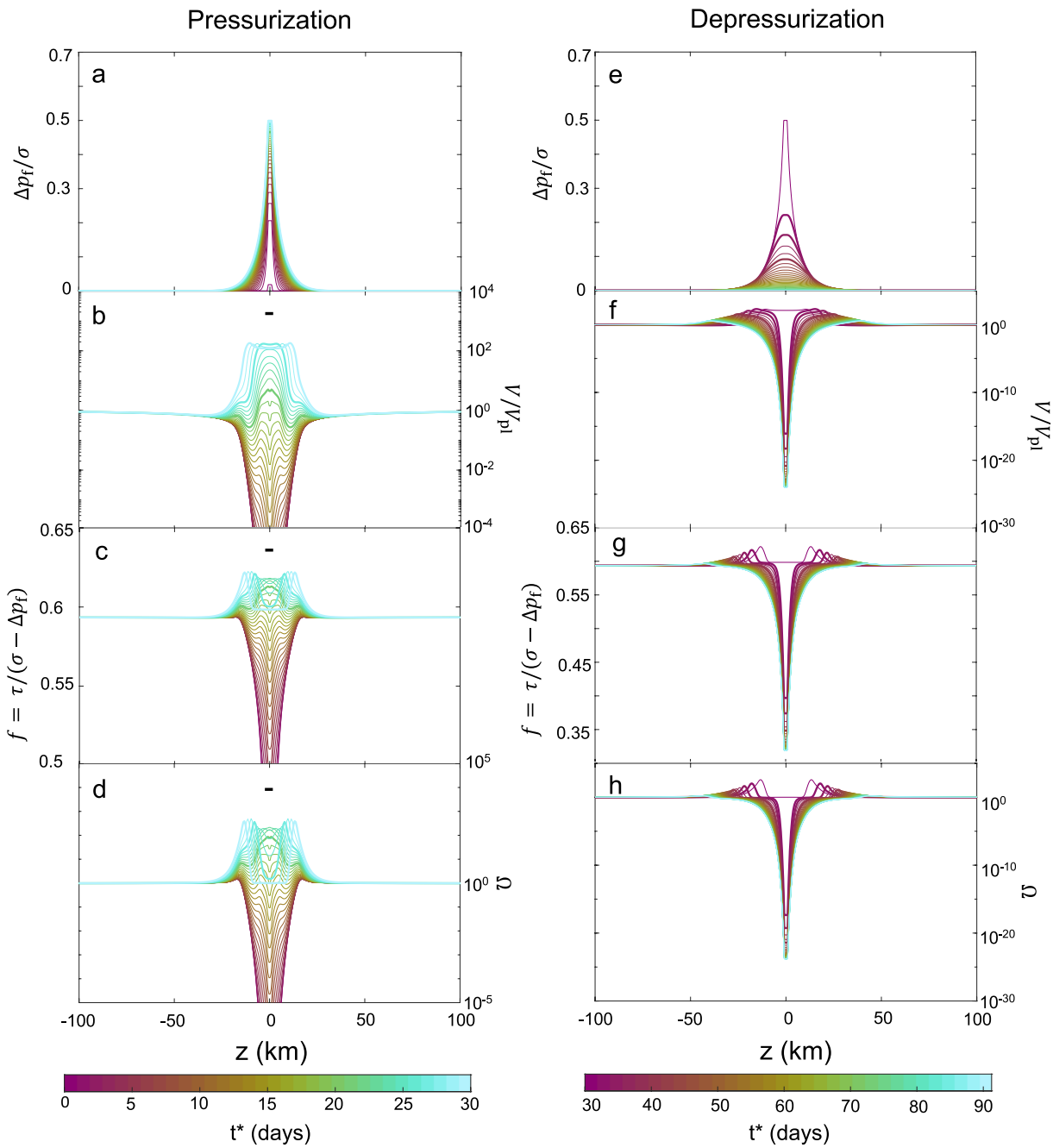

Figure 6. Profiles along depth showing the evolution of field variables $\Delta p_f/\sigma$, V/V_{pl}, f and Ω during an induced SSE in representative model under type II perturbation. $\Omega = V\theta/D_{RS}$ represents the proximity to steady state (Rubin & Ampuero, 2005). Thick black line in (b–d) shows the characteristic size of the process zone L_b. Contours are every ~1 day during pressurization and every ~2 days during depressurization. Bold contours correspond to the snapshots shown in Figures 3g–3l.

drop is again much lower than the applied pore-pressure change, which is attributable to the decrease of the shear stress at the start of the perturbations ($t \geq 20$ yr, Figure 5b) and to the fact that the perturbation period is too short for the shear stress to recover its value before the start of perturbations (at $t < 20$ yr).

4. Reproducing Shallow Gisborne SSEs

To find the parameter space that reproduces Gisborne SSE properties, we explore the perturbation amplitude and characteristic length, keeping the perturbation period constant ($T_{per} = 2$ yr). A limited range of parameters

are considered, as the exploration targets only Gisborne SSE properties, where pore-pressure cycling has been well characterized (Warren-Smith et al., 2019). For each simulation case, we calculate the average source properties of induced SSEs (i.e., duration, magnitude, maximum slip, and peak velocity), as described in Section 2.4. Note that during the parameter exploration, we set V_{thr} = 0.3 mm/day (Section 2.4), which is why SSEs have longer duration and higher magnitudes than constrained by observations at Hikurangi.

To investigate the effect of the perturbation amplitude on SSE properties, we explore Δp_{max} from 0.375 to 2.25 MPa ($0.125 \leq \Delta p_{max}/\sigma \leq 0.75$) for both perturbation types. The perturbation size is explored within different ranges for each perturbation type. For type I case, R_0 ranges from 11.25 to 45 km ($2.7 \leq R_0/L_b \leq 10.8$), while for type II, 1.6 km $< \sqrt{Dt_{inj}} <$ 11.4 km ($0.8 \leq \sqrt{Dt_{inj}}/L_b \leq 2.8$). In the latter case, we explore D from 5 to 50 m^2/s and keep t_{inj} = 30 days, which is within the range of shallow Hikurangi SSE duration (~6–34 days, Ikari et al., 2020).

Figure 7 summarizes the average peak slip rate, duration and magnitude of SSEs as a function of the perturbation length scale and amplitude for both type I (Figures 7a–7f) and type II (Figures 7g–7l) perturbations. These SSE properties increase with the perturbation size in both cases (Figures 7a–7c and Figures 7g–7i). For a given size of the perturbation, these properties also increase with the perturbation amplitude for type II perturbation (Figures 7j–7l). This is not the case for type I perturbation, where the perturbation amplitude has a relatively minor effect on such SSE properties (Figures 7d–7f). On the other hand, SSE maximum slip is insensitive to changes in the perturbation characteristics and remains constant (~10 cm) for all simulation cases shown in Figure 7 (Figure S3 in Supporting Information S1).

In all simulations presented so far, we keep a constant a/b = 1.25 (Table 1). To investigate the sensitivity of SSE properties to changes in this parameter, we explore a/b from 1.1 to 2.5, while keeping b and L_b constant. Larger a/b (i.e., more strengthening conditions) negatively correlate with SSE peak velocity, duration and magnitude (Figures 8a–8c), as expected. The maximum slip remains ~10 cm (Figure 8d), just as for the case with a/b = 1.25 (Figure S3 in Supporting Information S1). This occurs because the maximum slip mainly depends on the perturbation period and the plate rate, which are kept constant in this exploration.

The ratio D_b/D, which determines how fast pore pressure drops during depressurization, also affects the characteristics of induced SSEs although it is not a main controlling parameter. In Figure 7, we set D_b/D = 1.1 in all simulations. We explore the effect of D_b/D on SSE properties in Figure S4 in Supporting Information S1. Our results show that higher D_b/D induce SSEs with shorter duration and thus lower magnitude. This effect is intuitive since higher D_b/D implies a shorter duration of the perturbation. Note that we assume a higher D_b/D (=1.6) for the representative model under type II perturbation to better fit the short duration of shallow Gisborne SSEs.

In some simulation cases (not shown in Figure 7), SSE peak velocities alternate between slow and fast values (e.g., Figure S5 in Supporting Information S1). We refer to this behavior as 'slip-rate doubling'. Since similar observations have not been made on observed SSEs, we describe this phenomenon in the supplementary information (Text S2 in Supporting Information S1).

5. Reproducing the Source Properties of SSEs in Several Subduction Zones

To investigate whether our modeling approach could reproduce broader SSE properties, we explore further the perturbation characteristics. We consider a wider range of perturbation length scales than in Section 4 and explore the effect of the perturbation period and the velocity threshold (V_{thr}) on SSE properties. We focus here on SSE duration and moment, which are the first-order properties. Model parameters are as given in Table 1, with the difference that we increase the shear modulus and effective normal stress to account for the fact that many well-documented SSEs occur at deep depths (>20 km). Thus, we set μ = 30 GPa, consistent with models that target deep SSEs (e.g., Li & Liu, 2016; Matsuzawa et al., 2010) and, for simplicity, σ = 9 MPa, so that L_b remains the same (Table 1). In this section, we consider only type II (along-fault fluid diffusion) perturbation because it gives insight into the fault hydraulic properties required to generate SSEs comparable to observations using our modeling approach.

5.1. Exploration of Type-II Perturbation Characteristics

To explore a broad range of perturbation length scales, we vary D and t_{inj} over a few orders of magnitude, respectively 10^{-1} to 10^2 m^2/s and 10–$10^{2.9}$ days (or 0.027–2 yr), so that $10^{-1.15} \leq \sqrt{Dt_{inj}}/L_b < 10^{1.15}$. To isolate the

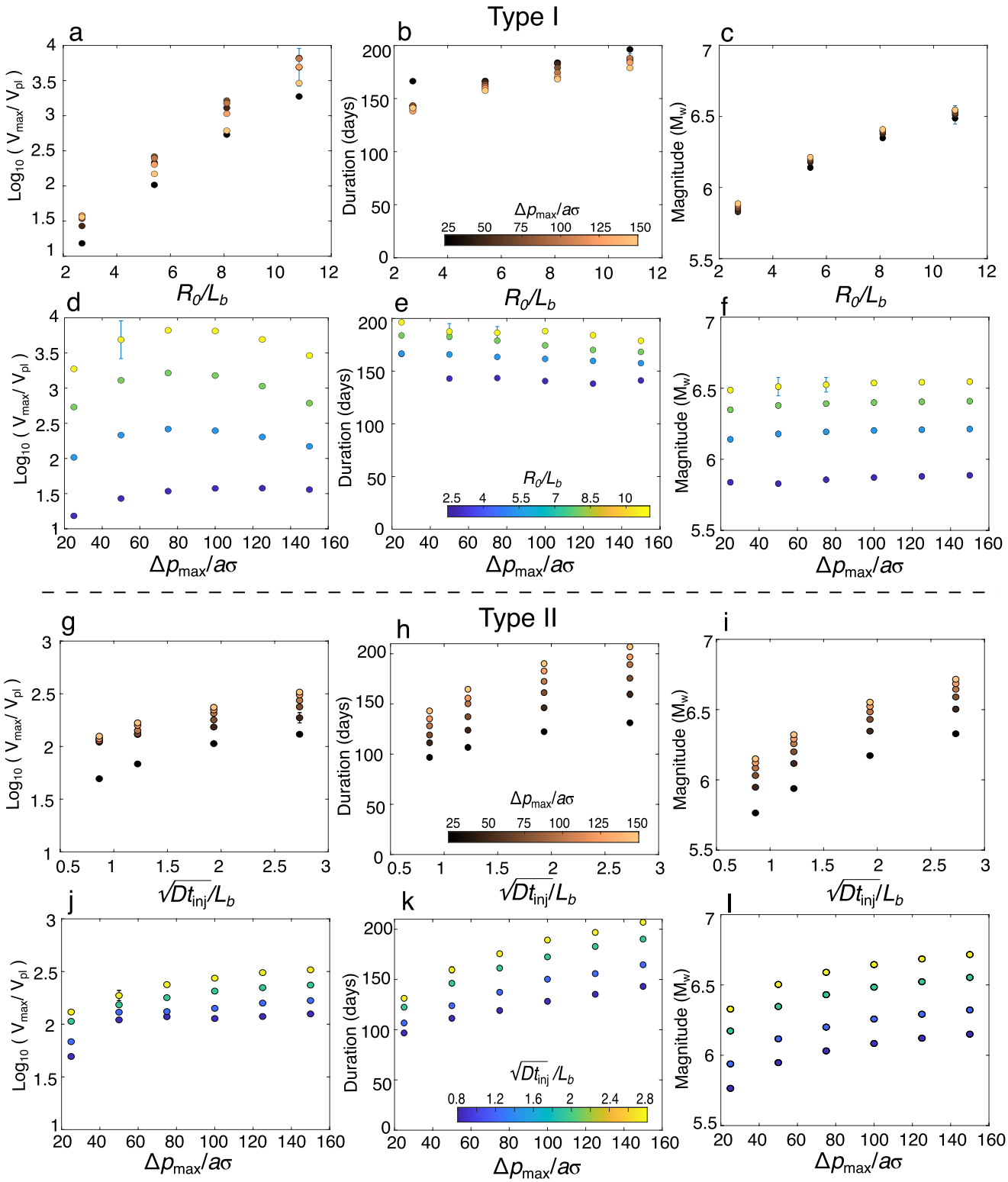

Figure 7. Average properties of slow slip events (SSEs) induced by periodic perturbations in pore-pressure of (a–f) type I and (g–l) type II. Model parameters are given in Table 1. SSE properties are shown as a function of (a–c, g–i) the perturbation length scale (R_0/L_b or $\sqrt{Dt_{\text{inj}}}/L_b$) for various values of the perturbation amplitude and as a function of (d–f, j–l) the perturbation amplitude ($\Delta p_{\max}/a\sigma$) for various values of the perturbation length scale. Vertical lines indicate standard deviation. For type II perturbation, we set $D_b/D = 1.1$ in all cases.

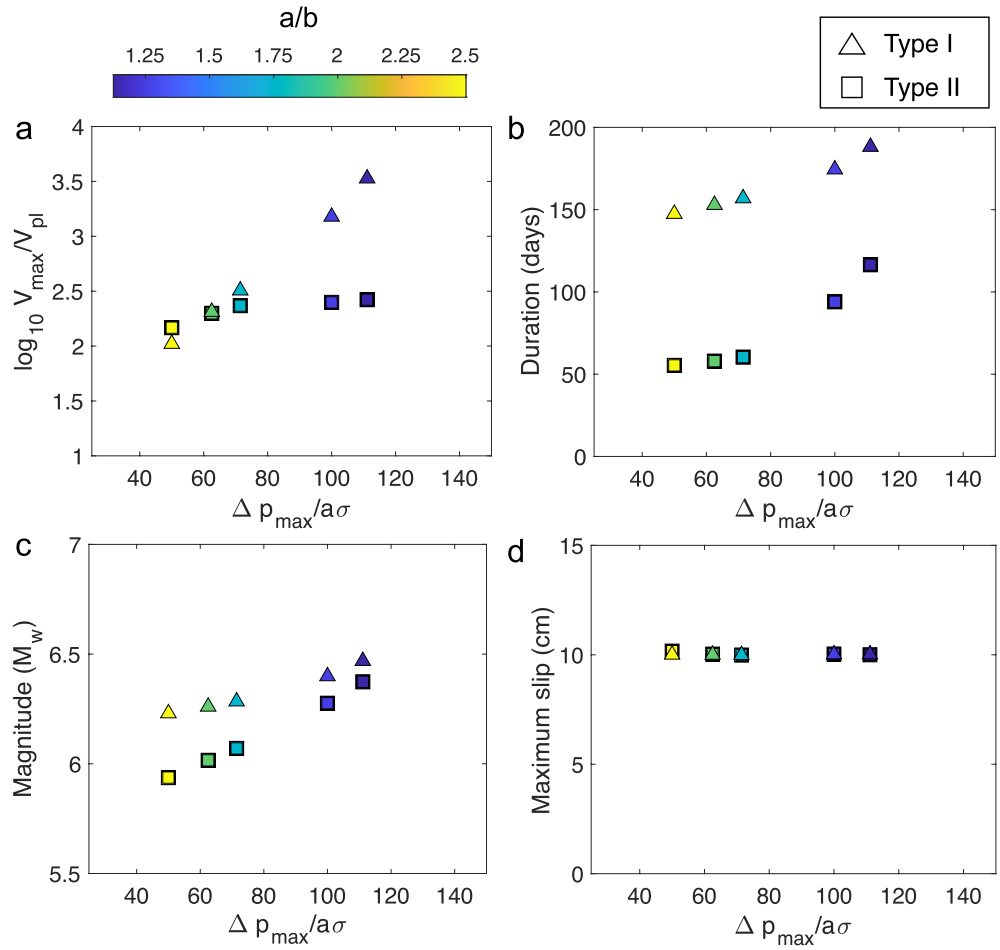

Figure 8. Exploration of a/b, a ranges from 0.0044 to 0.01 and $b = 0.004$. Average SSE properties: (a) maximum slip rate, (b) duration, (c) magnitude (M_w), and (d) maximum slip, are shown as a function of perturbation amplitude for type I (triangles) and type II (squares) perturbation. We consider the same perturbation characteristics of the representative models under type I and type II perturbation (Table 2); except that $\Delta p_{max} = 1.5$ MPa in type I case.

effect of $\sqrt{Dt_{inj}}/L_b$ on SSE properties, we set a constant $T_{per} = 5$ yr, $\Delta p_{max}/\sigma = 0.5$ and $V_{thr} = 0.3$ mm/day. To calculate SSE properties, we use the same approach described in Section 2.4. We plot the average moment and duration of induced SSEs in each simulation in Figure 9a. Note that for a given simulation, SSEs have the same properties after the first few perturbation cycles. Induced SSEs cover a broad range of durations and moments, from short duration (~40 days) and low magnitudes (~M_w5.5), to long duration (~1 yr) and large magnitude (~M_w8). The change in SSE properties positively correlates with $\sqrt{Dt_{inj}}/L_b$ (Figure 9a). Examining D and t_{inj} separately, we find that t_{inj} largely controls SSE duration while the magnitude of induced SSEs increases mainly with D.

As shown in Section 3, the period of the perturbation defines the recurrence interval of induced SSEs. Since observed SSE periodicity typically ranges from one to several years (Schwartz & Rokosky, 2007), we impose perturbations with periods ranging from 1 to 8 yr. For simplicity, we keep $t_{inj} = 0.5$ yr and vary D over the same range shown in Figure 9a. We find that for a given $\sqrt{Dt_{inj}}/L_b$, SSE duration and moment increase with the perturbation period (Figure 9c). This could be explained by the fact that the fault is strongly locked in the period between perturbations, despite the rate-strengthening condition. Thus, setting a longer perturbation period implies higher strain accumulation, which is released during pore-pressure increase, resulting in SSEs with longer duration and larger magnitude. We note that simulation cases with $D = 10$ or 100 m^2/s and $T_{per} = 1$ or 2 yr lead to slip-rate doubling (Text S2 in Supporting Information S1), and these results are not shown in Figure 9c.

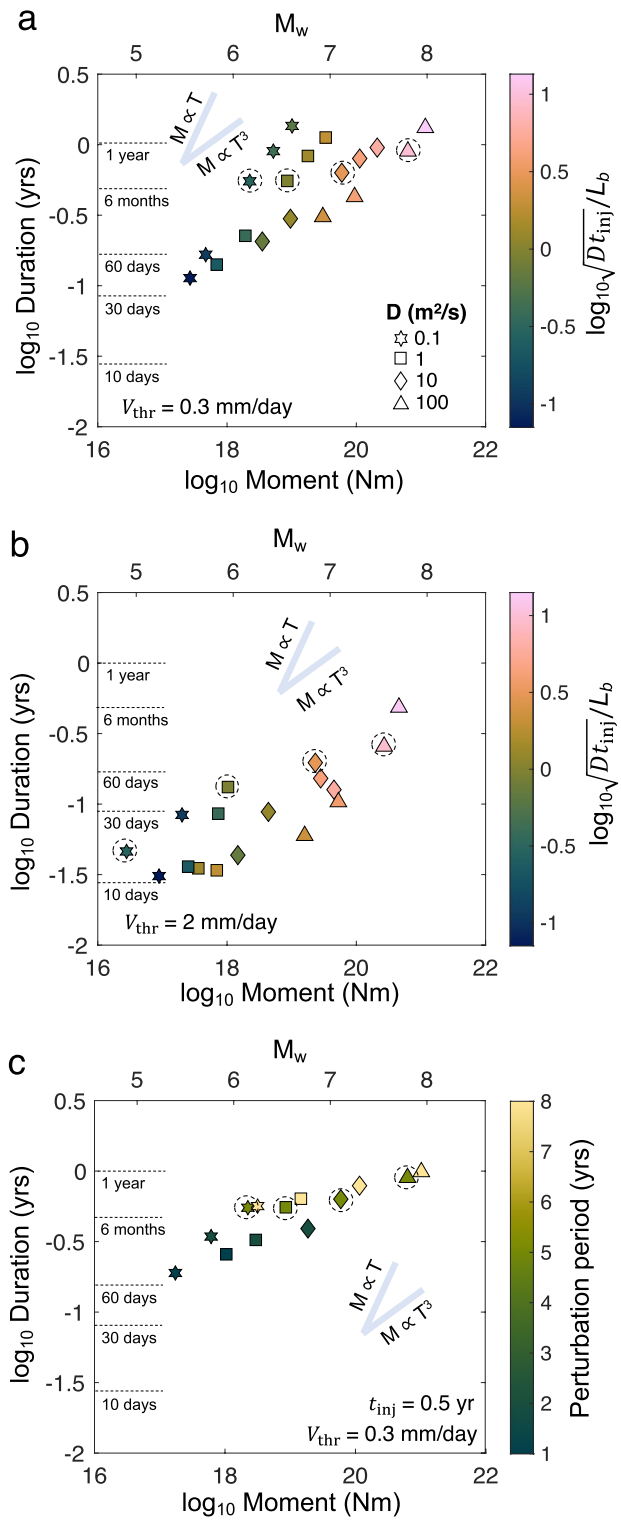

Figure 9. Source properties of induced slow slip events (SSEs) for simulation cases under type II perturbation. SSE moment-duration for cases with (a) different perturbation size $\sqrt{Dt_{inj}}/L_b$, (b) higher V_{thr} = 2 mm/yr for same cases shown in (a), and (c) different perturbation period (assuming t_{inj} = 0.5 yr). V_{thr} = 0.3 mm/day for (a) and (c). t_{inj} takes the values of 10 days, 30 days, 6 months, 1 year, and 2 years in (a) and (b); except for D = 100 m^2/s, where we do not consider t_{inj} = 2 yr. Dashed black circles indicate cases with the same perturbation characteristics. Markers' shape correspond to different diffusivity values (D) as shown in (a). For reference, the linear and cubic moment-duration scaling trends (thick gray lines in a to c) are also included. D_b/D = 3 in all cases, except for D = 100 m^2/s, where D_b/D = 1.5, since larger ratios led to slip-rate doubling (Text S2 in Supporting Information S1).

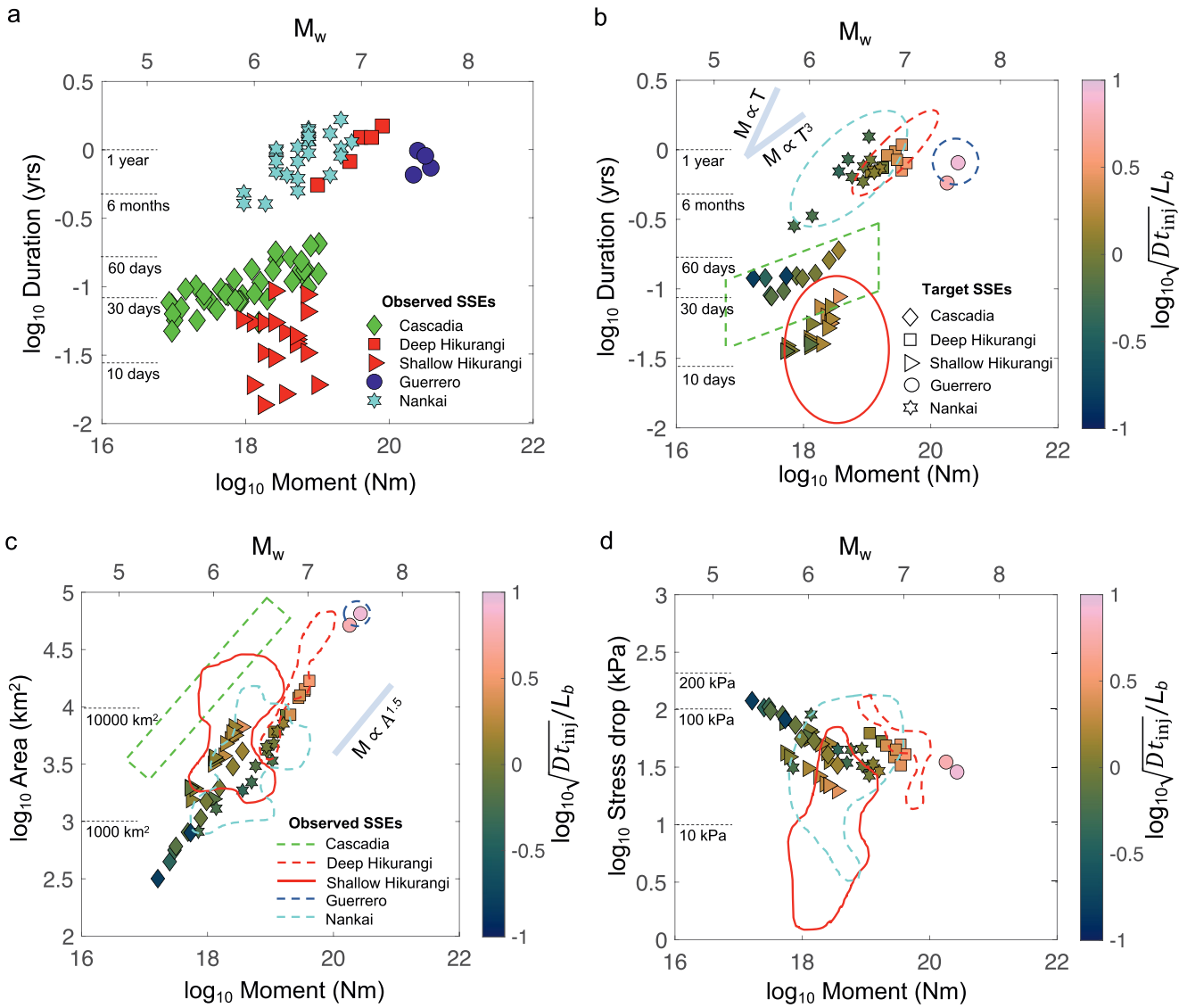

Figure 10. Comparison between observed and modeled source properties of slow slip events (SSEs) from different subduction zones. (a) Observed moment and duration of shallow and deep Hikurangi SSEs (Ikari et al., 2020), Cascadia SSEs (Michel et al., 2019), Nankai SSEs (Takagi et al., 2019) and Guerrero SSEs (Radiguet et al., 2012, 2016). For Cascadia SSEs, we plot the mean value between the minimum and maximum duration and moment estimations in Michel et al. (2019). Note that to compare observed Nankai SSE moments with our model results, we set $\mu = 30$ GPa, instead of 40 GPa, as reported by Takagi et al. (2019). (b–d) Source properties of induced SSEs in simulation cases with different $\sqrt{Dt_{inj}}/L_b$ (see also Table 4 and Figure S7 and Table S2 in Supporting Information S1). Each shape corresponds to a different target SSE as shown in (b). The colored lines highlight the range of observed properties for a given target SSE, as shown in (c). For reference, the moment-duration and moment-area scaling trends (thick gray lines in b and c) are also included. Note that only stress drop for SSEs along Hikurangi (Ikari et al., 2020) and Nankai (Takagi et al., 2019) subduction zones were constrained by observations. For deep Hikurangi SSEs, we take the average stress drop between the different stages of the event shown in the catalog from Ikari et al. (2020).

Apart from the perturbation characteristics, the ability of onshore GPS networks to detect slip also affects the estimated SSE duration and moment. In Figures 9a and 9c, we calculate SSE properties assuming $V_{thr} = 0.3$ mm/day, which is a relatively low threshold (Section 2.4). For comparison in Figure 9b, we consider a higher threshold, $V_{thr} = 2$ mm/day and calculate SSE properties for the same simulation cases as in Figure 9a. As expected, SSEs have shorter durations and lower magnitudes than estimated using the lower detection threshold (cf. Figures 9a and 9b). Note that only three simulation cases with $D = 0.1$ m^2/s are shown in Figure 9b, as for the other two cases SSE peak velocities fall below V_{thr}.

As mentioned in Section 2.3.2, $r_0 = 1$ km in all simulation cases. Varying this parameter has a minor effect on the perturbation characteristics and induced SSE properties (Figure S6 in Supporting Information S1).

Table 4
Plate Rate (V_{pl}) and Velocity Threshold (V_{thr}) Assumed for Each Target Slow Slip Events (SSEs)

Target SSEs	V_{pl} (mm/yr)	V_{thr}/V_{pl}	V_{thr} in mm/day
Shallow Hikurangi	50 or 40[a]	15	2 or 1.6
Deep Hikurangi	40	3	0.33
Cascadia	40	3	0.33
Nankai	67	3	0.55
Guerrero	61	3	0.5

Note. V_{thr} represents the slip velocity threshold assumed to calculate SSE properties (Section 2.4). The highest V_{thr} (15 V_{pl}) is assumed for shallow Hikurangi SSEs, as they occur offshore, away from GPS networks. We set $V_{thr} = 3\ V_{pl}$ for all SSEs that occur beneath GPS networks. We take V_{pl} from (Hikurangi) Wallace et al. (2004), (Cascadia) McCaffrey et al. (2013), (Nankai) Miyazaki and Heki (2001), and (Guerrero) DeMets et al. (2010).
[a]We set $V_{pl} = 40$ mm/yr for southern Hikurangi margin (south of Hawkes Bay) and $V_{pl} = 50$ mm/yr for northern Hikurangi (offshore Gisborne), consistent with the change in convergence rates along the margin (Wallace et al., 2004).

5.2. Comparison to Observed SSE Moment and Duration

In this section, we simulate the moment and duration of SSEs in different subduction zones to constrain the parameter space within our modeling approach that captures first-order SSE properties. We target short-term (i.e., short-duration, low magnitude) SSEs from Cascadia (Michel et al., 2019) and shallow Hikurangi (including SSEs along the whole margin, not only offshore Gisborne) subduction zones, and long-term (i.e., long-duration, large magnitude) SSEs from deep Hikurangi (Ikari et al., 2020; Wallace, 2020), Guerrero (Mexico) (Radiguet et al., 2012) and Nankai (Takagi et al., 2019) subduction zones (Figure 10a). While pore-pressure fluctuations have not been associated with deep Hikurangi SSEs nor long-term Nankai SSEs, we include them here to explore the possibility that these SSEs are also induced by perturbations in pore pressure.

To reproduce the observed SSE duration and moment, we tune the perturbation length scale, period and amplitude, where the perturbation period corresponds to the approximate recurrence interval of observed SSEs. Table S2 in Supporting Information S1 shows the perturbation characteristics for each simulation case. Note that we also vary D_b/D to better fit the duration of target SSEs. For each target SSE, we define V_{pl} and V_{thr} as shown in Table 4. We consider $V_{thr} = 3V_{pl}$ for deep SSEs in Cascadia, Nankai and Hikurangi, to account for the fact that deep SSEs occur beneath geodetic networks, where the resolution is relatively high (e.g., 2.2–4.5 V_{pl}; Wech & Bartlow, 2014). We plot the average duration and moment of modeled SSEs in Figure 10b. Modeled SSEs broadly capture the observed SSE durations and moments (colored lines in Figure 10b). This agreement is remarkable, given that these models are relatively simple. However, the model fails to reproduce the shortest-duration (≤10 days) shallow Hikurangi SSEs. A broader parameter exploration may be needed to find models that capture SSEs with such properties. Note that even though we compare our results with individual SSEs, the models are more representative of repeating (i.e., with the same properties) SSEs.

The trends seen in Figures 9a–9c can also be distinguished in Figure 10b. Guerrero SSEs, which exhibit the largest magnitudes and durations, arise in simulation cases with the largest perturbation size ($0.78 \le \log_{10}\sqrt{Dt_{inj}}/L_b \le 0.93$). In contrast, lower-magnitude ($M_w < 6.8$) SSEs in Nankai, Cascadia and shallow Hikurangi require smaller perturbation sizes ($\log_{10}\sqrt{Dt_{inj}}/L_b \le 0.44$). Interestingly, shallow Hikurangi SSEs, which exhibit the shortest durations, call for larger perturbations ($-0.15 \le \log_{10}\sqrt{Dt_{inj}}/L_b \le 0.44$) than Cascadia and Nankai SSEs ($-0.8 \le \log_{10}\sqrt{Dt_{inj}}/L_b \le 0.15$). This is consistent with the use of a higher V_{thr} (Table 4), which causes SSE duration and moment to be underestimated. We also notice that the difference between induced SSEs of short and long duration is mainly due to the duration of pressurization (t_{inj}), consistent with Figure 9a. For short-duration SSEs, $t_{inj} \le 30$ days, while for most long-duration SSEs, $t_{inj} \ge 6$ months (Table S2 in Supporting Information S1).

To further constrain our results, we calculate the area and stress drop of modeled SSEs and compare them to available observations (Figures 10c and 10d; see also Figure S7 in Supporting Information S1). Modeled SSE areas partially overlap those estimated by observations, excluding Cascadia SSEs (Figure 10c). The model does not capture Cascadia SSE areas because they are markedly elongated, while simulated SSE areas are nearly circular. The stress drops of modeled SSEs range from ~20–120 kPa (Figure 10d). Modeled SSE stress drops capture those constrained by observations of Nankai SSEs (Takagi et al., 2019). However, they only partially overlap those from shallow and deep Hikurangi SSEs (red lines in Figure 10d).

6. Discussion

Our results show that periodic pore-pressure perturbations on a rate-strengthening fault zone induce SSEs broadly consistent with observations. SSEs arise over a range of rate-strengthening conditions ($1.1 < a/b \le 2.5$, Figure 8), perturbation length scales ($2 < R_0/L_b < 12$ and $-1.1 \le \log_{10}\sqrt{Dt_{inj}}/L_b \le 1.1$, Figures 7, 9, and 10) and pore pressure amplitudes ($0.1 < \Delta p_{max}/\sigma < 0.8$, Figure 7). The source properties of induced SSEs (duration, magnitude,

slip rate, recurrence interval) vary with the perturbation characteristics (length scale, amplitude, and period, Figures 7 and 9). After exploring two types of pore-pressure perturbations that model either a simplified (type I) or along-fault (type II) fluid migration, we find models that induce SSEs with source properties comparable to those of shallow Hikurangi SSEs (Table 3). The fact that both perturbation types capture the characteristics of these events highlights the non-uniqueness of the model results. Using type II perturbation, the model captured the observed moment and duration of short-term SSEs in Cascadia and Hikurangi (except for Hikurangi SSEs with very short durations, <10 days), and long-term SSEs in Nankai, Hikurangi and Guerrero (Figure 10b). These results suggest that pore-pressure cycling may be a viable mechanism to generate SSEs on rate-strengthening faults.

Pore pressure evolution is markedly different between type I and II perturbations. In the former, the temporal evolution of pore pressure has the same pattern inferred within the lower plate along the Hikurangi margin (Section 2.3.1), which implies that the lower plate and the interface shear zone are hydrologically coupled. However, for the type II model, the increase in pore pressure in the plate interface is delayed and more rapid that the steady increase inferred within the slab, meaning that during the interseismic period (prior to injection) the lower plate and interface are hydrologically decoupled. Given the non-uniqueness of the model results, we cannot distinguish between these two scenarios. Likewise, it is also unclear whether near-lithostatic pore pressure changes are required to induce SSEs. For both representative models of shallow Gisborne SSEs, sub-lithostatic pore pressure changes, $\Delta p_{max}/\sigma = 0.625$ (type I) or 0.5 (type II), induced SSEs comparable to observations (Table 2). We compare $\Delta p_{max}/\sigma$ with inferred pore pressure changes during SSEs by scaling σ to reasonable values for shallow Hikurangi SSEs (10–30 MPa; Arnulf et al., 2021), which gives a Δp_{max} of 6.25–18.75 MPa (type I) or 5–15 MPa (type II). Both ranges are comparable to or slightly larger than the estimated change in pore pressure during SSEs (~1–10 MPa; Gosselin et al., 2020). Observational constraints on the hydrological coupling between the lower plate and the plate interface are needed to validate these models.

Our model results indicate that hydraulic diffusivity values in the range of 0.1–100 m^2/s are required to generate SSEs comparable to observations (Table S2 in Supporting Information S1). These values are several orders of magnitude larger than laboratory and in-situ measurements in the fault zone —the highest in-situ value reported inside a fault zone being 0.024 m^2/s (Xue et al., 2013). According to our model results, hitherto estimated hydraulic diffusivity values would lead to short perturbation length scales, insufficient to generate detectable ($>M_w5$) SSEs. Considering an upper bound with $D = 0.024$ m^2/s (Xue et al., 2013), the length scale of the perturbation ($\sqrt{Dt_{inj}}/L_b$) would be half the minimum perturbation length constrained by our results ($D = 0.1$ m^2/s, Figure 9a), assuming the same t_{inj} and L_b. Even though the extremely high hydraulic diffusivity values implied by our model are difficult to reconcile with current estimates, they may be explained by transient and localized changes in fault zone properties before and during slow slip, which may be induced by fractures during slip (Miller, 2015), hydrofracturing (Muñoz-Montecinos et al., 2021) or porosity waves (Skarbek & Rempel, 2016). However, the time scale of these *transient* changes are uncertain, and they may not occur over the entire duration of SSEs, as assumed in our model. Indirect observations of fluid migration during slow slip have inferred that fault zone permeability increases during SSEs in Mexico (3.6×10^{-12} m^2, Frank et al., 2015) and the Tokai region (10^{-18} to 10^{-15} m^2; Tanaka et al., 2010, 2018). For comparison, we estimate permeability through the relation $k = D\eta\beta\phi$, where the permeability (k) depends on fluid viscosity (η), porosity (ϕ), the sum of pore and fluid compressibility (β) and the hydraulic diffusivity (D); the latter which we take from our model results (Table S2 in Supporting Information S1). We consider the approximate order of magnitude of these parameters, where $\eta = 10^{-3}$ Pa s (Cheng, 2016), $\beta = 10^{-8}$ Pa^{-1} (within the range in Mase & Smith, 1987; Rice, 2006; Wibberley, 2002) and, for simplicity we set $\phi = 0.05$, noting that ϕ may range from ~10^{-2} to 10^{-1} (Peacock et al., 2011; Saffer & Tobin, 2011; Segall & Rice, 1995). The estimated permeability ranges from 5×10^{-14} to 5×10^{-11} m^2 (Table 5). Although there is a partial overlap with inferred permeability ranges during SSEs, our estimates are still higher than these values. This discrepancy could be attributed to several reasons: (a) Observations have not constrained the full range of permeability changes during slow slip. Thus, in situ measurements of hydraulic properties within the slow slip fault zone will be required to validate these results. (b) Pore pressure fluctuations in rate-strengthening faults may not be sufficient on their own to induce SSEs comparable to observations and other elements are at play. For instance, it is plausible that SSEs require rate-weakening friction to nucleate (e.g., Liu & Rice, 2007; Shibazaki & Shimamoto, 2007), and pore pressure changes facilitate the propagation of aseismic slip. (c) A more complex model, which accounts for other factors (e.g., porosity evolution, multiple fluid sources) may be required to constrain the permeability changes during slow slip.

Table 5
Estimation of Fault Zone Permeability (k) Through the Relation $k = D\eta\beta\phi$, Assuming Uniform $\eta = 10^{-3}$ Pa·s (Fluid Viscosity), $\beta = 10^{-8}$ Pa^{-1} (Effective Compressibility) and $\phi = 0.05$ (Porosity)

Target SSEs	D (m^2/s)	$k = D\eta\beta\phi$ (m^2)
Shallow Hikurangi	10	5E−12
	25	1.25E−11
	50	2.5E−11
	60	3E−11
	75	3.75E−11
	100	5E−11
Deep Hikurangi	1	5E−13
	2	1E−12
	2.5	1.25E−12
Cascadia	0.5	2.5E−13
	1	5E−13
	5	2.5E−12
	10	5E−12
	20	1E−11
	30	1.5E−11
	40	2E−11
Nankai	0.1	5E−14
	0.25	1.25E−13
	0.5	2.5E−13
Guerrero	20	1E−11

Note. We set the same hydraulic diffusivity (D) required to reproduce SSE duration and magnitude with our model (Table S2 in Supporting Information S1).

The stress drop of modeled target SSEs ranges from ~20–120 kPa (Figure 10d), which is broadly consistent with the range estimated in a worldwide compilation of SSE source parameters (10–1,000 kPa; Gao et al., 2012). These results are intriguing as these values are only a fraction (<0.03) of the maximum applied pore-pressure change (1.5–4.5 MPa, Table S2 in Supporting Information S1), which is consistent with observations in that inferred pore pressure change (~1–10 MPa; Gosselin et al., 2020) is larger than typical SSE stress drop. In our model, this occurs because the shear stress distribution changes in the fault plane in response to periodic pore-pressure changes (Section 3). Within the pressurized area, shear stress decreases in proportion to the pore pressure increase at the start of the perturbations (Figure 5b). Notably, the shear stress does not return to its initial (i.e., before the onset of perturbations) value in the inter-SSE period (Figure 5b), as the perturbation period is not long enough for the shear stress to recover completely.

The scaling relations of SSEs have elicited considerable debate due to their association with the mechanics of slow slip. Initially, SSE moment-duration scaling was suggested to follow a linear trend ($M \propto T$; Ide et al., 2007), while recent observations indicated a cubic trend to be more suitable ($M \propto T^3$; Michel et al., 2019; Frank & Brodsky, 2019; Tan & Marsan, 2020). Definite moment-duration scaling trends are not distinguishable in our model results (Figures 9a, 9b, and 10b). Only simulation cases with a given D exhibit trends that range from linear to cubic (Figures 9a and 9c). However, this is not the case for modeled target SSEs, where scaling trends are varied (Figure 10b). Thus, our model results are inconclusive regarding the existence of SSE moment-duration scaling. On the other hand, modeled target SSEs follow a distinct moment-area scaling close to $M \propto A^{1.5}$ (Figure 10c), which is the same as for SSEs in Cascadia (Michel et al., 2019) and regular earthquakes (Kanamori & Anderson, 1975).

Our modeling approach has several limitations. (a) Induced SSEs exhibit a roughly circular slip distribution. Such simplification would be valid for some SSEs (e.g., shallow Hikurangi SSEs, Guerrero SSEs), while it is not appropriate for elongated SSEs observed in other subduction zones (e.g., Cascadia). (b) The model predicts very low slip velocities during the inter-SSE period, with some falling below the range constrained by RSF. (c) Our approach does not consider the complexity of fluid transport processes, which depend on several factors, such as fault zone structure, temperature, and lithology (Saffer & Tobin, 2011). Accounting for such complexities may be required to understand the effect of pore pressure on SSEs in diverse environments. (d) Our model only accounts for a one-way coupling between pore pressure and fault slip. Although this is useful as a first-order approximation, previous models have emphasized that porosity and permeability evolution, including permeability enhancement, may significantly affect fluid-induced slip (e.g., Bhattacharya & Viesca, 2019; Cappa et al., 2018; Yang & Dunham, 2021). (e) The model does not account for the effect of the free surface, which induces normal stress changes on the fault. Such effect may be important for reproducing the behavior of shallow SSEs (Ohtani & Hirahara, 2015). (f) We do not explain the mechanism whereby pore-pressure cycling occurs. Even though several mechanisms have been proposed to couple fault slip and fluid processes (e.g., Bernaudin & Gueydan, 2018; Farge et al., 2021; Skarbek & Rempel, 2016; Zhu et al., 2020), it is still uncertain which one governs pore-pressure fluctuations during SSEs. (g) Finally, we do not explore the full fault response under RSF; other state evolution laws are not considered, such as the slip law (Ruina, 1983) or composite laws (Kato & Tullis, 2001). Rate-weakening behavior is not explored either.

Our model results indicate that rate-strengthening faults are very sensitive to pore-pressure perturbations. SSEs arise after pore pressure perturbations with a broad range of characteristics (Figures 7, 9, and 10). Likewise, perturbations on faults with different rate-strengthening conditions lead to SSEs (Figure 8). These results suggest that rate-strengthening friction properties may play a more important role in slow slip generation than commonly assumed. In addition, the emergence of SSEs within our modeling approach is not limited by a critical nucleation

size, in contrast with widely used models based on rate–weakening faults (e.g., Liu & Rice, 2007), suggesting a broader range of conditions favorable for SSE occurrence.

7. Conclusions

Using a relatively simple model approach in which fault slip relates to pore-pressure changes through changes in effective stress (i.e., one-way coupling), we show that periodic pore-pressure perturbations on a rate-strengthening fault zone induce SSEs with characteristics comparable to observations. Source properties of induced SSEs (duration, magnitude, slip rate, recurrence interval) vary with the perturbation characteristics (length scale, amplitude, and period). By exploring such characteristics, we find models that broadly capture the properties (duration, magnitude, recurrence interval, and slip) of shallow Hikurangi SSEs and the moment and duration of SSEs in other subduction zones. The stress drops of modeled SSEs range from ∼20 to 120 kPa while the amplitudes of pore-pressure perturbations is several MPa, broadly consistent with those inferred from observations. Our model results indicate that hydraulic diffusivities between 0.1 and 100 m^2/s are required to generate SSEs comparable to observations. Such values are several orders of magnitude larger than estimated hydraulic diffusivity from the laboratory or in-situ measurements and correspond to permeabilities of $\sim 10^{-14}$ to 10^{-10} m^2. Future constraints on in-situ values of fault hydraulic properties during SSEs are needed to test the model predictions. Our results indicate that pore-pressure cycling may be a viable mechanism to generate SSEs on rate-strengthening faults.

Data Availability Statement

The numerical data used to produce the figures is available at https://doi.org/10.5281/zenodo.7796680.

Acknowledgments
This work was supported by the Rutherford Discovery Fellowship from the Royal Society of New Zealand and the Ministry of Business, Innovation and Employment (MBIE) grant to GNS (contract CO5X1605), a Marsden Fund Grant (GNS20-01), and JSPS KAKENHI (21H05206). Computing resources were provided by the New Zealand eScience Infrastructure (NeSI) high-performance computing facilities. We thank the Associate Editor and two anonymous reviewer's for their valuable and detailed feedback, which helped improve the quality of the manuscript. We also thank Eric Dunham and Alexis Saez for their suggestions in the modeling of the radial diffusion perturbation. Most figures use perceptually uniform color palettes from Crameri (2018). Open access publishing facilitated by Victoria University of Wellington, as part of the Wiley - Victoria University of Wellington agreement via the Council of Australian University Librarians.

References

Ampuero, J.-P., & Rubin, A. M. (2008). Earthquake nucleation on rate and state faults–Aging and slip laws. *Journal of Geophysical Research*, *113*(B1), B01302. https://doi.org/10.1029/2007JB005082

Arnulf, A. F., Biemiller, J., Lavier, L., Wallace, L. M., Bassett, D., Henrys, S., et al. (2021). Physical conditions and frictional properties in the source region of a slow-slip event. *Nature Geoscience*, *14*(5), 334–340. https://doi.org/10.1038/s41561-021-00741-0

Audet, P., Bostock, M. G., Christensen, N. I., & Peacock, S. M. (2009). Seismic evidence for overpressured subducted oceanic crust and megathrust fault sealing. *Nature*, *457*(7225), 76–78. https://doi.org/10.1038/nature07650

Behr, W. M., & Bürgmann, R. (2021). What's down there? The structures, materials and environment of deep-seated slow slip and tremor. *Philosophical Transactions of the Royal Society A: Mathematical, Physical & Engineering Sciences*, *379*(2193), 20200218. https://doi.org/10.1098/rsta.2020.0218

Bernaudin, M., & Gueydan, F. (2018). Episodic tremor and slip explained by fluid-enhanced microfracturing and sealing. *Geophysical Research Letters*, *45*(8), 3471–3480. https://doi.org/10.1029/2018GL077586

Bhattacharya, P., & Viesca, R. C. (2019). Fluid-induced aseismic fault slip outpaces pore-fluid migration. *Science*, *364*(6439), 464–468. https://doi.org/10.1126/science.aaw7354

Boulton, C., Niemeijer, A. R., Hollis, C. J., Townend, J., Raven, M. D., Kulhanek, D. K., & Shepherd, C. L. (2019). Temperature-dependent frictional properties of heterogeneous Hikurangi Subduction Zone input sediments, ODP Site 1124. *Tectonophysics*, *757*, 123–139. https://doi.org/10.1016/j.tecto.2019.02.006

Bürgmann, R. (2018). The geophysics, geology and mechanics of slow fault slip. *Earth and Planetary Science Letters*, *495*, 112–134. https://doi.org/10.1016/j.epsl.2018.04.062

Cappa, F., Guglielmi, Y., Nussbaum, C., & Birkholzer, J. (2018). On the relationship between fault permeability increases, induced stress perturbation, and the growth of aseismic slip during fluid injection. *Geophysical Research Letters*, *45*(20), 11012–11020. https://doi.org/10.1029/2018GL080233

Cappa, F., Scuderi, M. M., Collettini, C., Guglielmi, Y., & Avouac, J.-P. (2019). Stabilization of fault slip by fluid injection in the laboratory and in situ. *Science Advances*, *5*(3), eaau4065. https://doi.org/10.1126/sciadv.aau4065

Carslaw, H., & Jaeger, J. (1959). *Conduction of heat in solids*. Clarendon Press.

Cheng, A. H.-D. (2016). *Poroelasticity* (Vol. 27). Springer International Publishing. https://doi.org/10.1007/978-3-319-25202-5

Condit, C. B., & French, M. E. (2022). Geologic evidence of lithostatic pore fluid pressures at the base of the subduction seismogenic zone. *Geophysical Research Letters*, *49*(12), e2022GL098862. https://doi.org/10.1029/2022GL098862

Crameri, F. (2018). Geodynamic diagnostics, scientific visualisation and StagLab 3.0. *Geoscientific Model Development*, *11*(6), 2541–2562. https://doi.org/10.5194/gmd-11-2541-2018

Cruz-Atienza, V. M., Villafuerte, C., & Bhat, H. S. (2018). Rapid tremor migration and pore-pressure waves in subduction zones. *Nature Communications*, *9*(1), 2900. https://doi.org/10.1038/s41467-018-05150-3

Dal Zilio, L., Lapusta, N., & Avouac, J.-P. (2020). Unraveling scaling properties of slow-slip events. *Geophysical Research Letters*, *47*(10), e2020GL087477. https://doi.org/10.1029/2020GL087477

DeMets, C., Gordon, R. G., & Argus, D. F. (2010). Geologically current plate motions. *Geophysical Journal International*, *181*(1), 1–80. https://doi.org/10.1111/j.1365-246X.2009.04491.x

Dieterich, J. H. (1979). Modeling of rock friction: 1. Experimental results and constitutive equations. *Journal of Geophysical Research*, *84*(B5), 2161–2168. https://doi.org/10.1029/JB084iB05p02161

Dublanchet, P. (2019). Fluid driven shear cracks on a strengthening rate-and-state frictional fault. *Journal of the Mechanics and Physics of Solids*, *132*, 103672. https://doi.org/10.1016/j.jmps.2019.07.015

Eijsink, A. M., & Ikari, M. J. (2022). Plate-rate frictional behavior of sediment inputs to the Hikurangi subduction margin: How does lithology control slow slip events? *Geochemistry, Geophysics, Geosystems*, *23*(6), e2022GC010369. https://doi.org/10.1029/2022GC010369

Farge, G., Jaupart, C., & Shapiro, N. M. (2021). Episodicity and migration of low frequency earthquakes modeled with fast fluid pressure transients in the permeable subduction interface. *Journal of Geophysical Research: Solid Earth*, *126*(9), e2021JB021894. https://doi.org/10.1029/2021JB021894

Frank, W. B., & Brodsky, E. E. (2019). Daily measurement of slow slip from low-frequency earthquakes is consistent with ordinary earthquake scaling. *Science Advances*, *5*(10), eaaw9386. https://doi.org/10.1126/sciadv.aaw9386

Frank, W. B., Shapiro, N. M., Husker, A. L., Kostoglodov, V., Bhat, H. S., & Campillo, M. (2015). Along-fault pore-pressure evolution during a slow-slip event in Guerrero, Mexico. *Earth and Planetary Science Letters*, *413*, 135–143. https://doi.org/10.1016/j.epsl.2014.12.051

Gao, H., Schmidt, D. A., & Weldon, R. J. (2012). Scaling relationships of source parameters for slow slip events. *Bulletin of the Seismological Society of America*, *102*(1), 352–360. https://doi.org/10.1785/0120110096

Gosselin, J. M., Audet, P., Estève, C., McLellan, M., Mosher, S. G., & Schaeffer, A. J. (2020). Seismic evidence for megathrust fault-valve behavior during episodic tremor and slip. *Science Advances*, *6*(4), eaay5174. https://doi.org/10.1126/sciadv.aay5174

Guglielmi, Y., Cappa, F., Avouac, J.-P., Henry, P., & Elsworth, D. (2015). Seismicity triggered by fluid injection-induced aseismic slip. *Science*, *348*(6240), 1224–1226. https://doi.org/10.1126/science.aab0476

Heimisson, E. R., Dunham, E. M., & Almquist, M. (2019). Poroelastic effects destabilize mildly rate-strengthening friction to generate stable slow slip pulses. *Journal of the Mechanics and Physics of Solids*, *130*, 262–279. https://doi.org/10.1016/j.jmps.2019.06.007

Hyndman, R. D., & Peacock, S. M. (2003). Serpentinization of the forearc mantle. *Earth and Planetary Science Letters*, *212*(3–4), 417–432. https://doi.org/10.1016/S0012-821X(03)00263-2

Ide, S., Beroza, G. C., Shelly, D. R., & Uchide, T. (2007). A scaling law for slow earthquakes. *Nature*, *447*(7140), 76–79. https://doi.org/10.1038/nature05780

Ikari, M. J., Marone, C., Saffer, D. M., & Kopf, A. J. (2013). Slip weakening as a mechanism for slow earthquakes. *Nature Geoscience*, *6*(6), 468–472. https://doi.org/10.1038/ngeo1818

Ikari, M. J., Wallace, L. M., Rabinowitz, H. S., Savage, H. M., Hamling, I. J., & Kopf, A. J. (2020). Observations of laboratory and natural slow slip events: Hikurangi subduction zone, New Zealand. *Geochemistry, Geophysics, Geosystems*, *21*(2), e2019GC008717. https://doi.org/10.1029/2019GC008717

Kanamori, H., & Anderson, D. L. (1975). Theoretical basis of some empirical relations in seismology. *Bulletin of the Seismological Society of America*, *65*(5), 1073–1095.

Kaneko, Y., Avouac, J.-P., & Lapusta, N. (2010). Towards inferring earthquake patterns from geodetic observations of interseismic coupling. *Nature Geoscience*, *3*(5), 363–369. https://doi.org/10.1038/ngeo843

Kato, N., & Tullis, T. E. (2001). A composite rate-and state-dependent law for rock friction. *Geophysical Research Letters*, *28*(6), 1103–1106. https://doi.org/10.1029/2000GL012060

Kita, S., Houston, H., Yabe, S., Tanaka, S., Asano, Y., Shibutani, T., & Suda, N. (2021). Effects of episodic slow slip on seismicity and stress near a subduction-zone megathrust. *Nature Communications*, *12*(1), 7253. https://doi.org/10.1038/s41467-021-27453-8

Lapusta, N., & Liu, Y. (2009). Three-dimensional boundary integral modeling of spontaneous earthquake sequences and aseismic slip. *Journal of Geophysical Research*, *114*(B9), B09303. https://doi.org/10.1029/2008JB005934

Larochelle, S., Lapusta, N., Ampuero, J., & Cappa, F. (2021). Constraining fault friction and stability with fluid-injection field experiments. *Geophysical Research Letters*, *48*(10), e2020GL091188. https://doi.org/10.1029/2020GL091188

Li, D., & Liu, Y. (2016). Spatiotemporal evolution of slow slip events in a nonplanar fault model for northern Cascadia subduction zone. *Journal of Geophysical Research: Solid Earth*, *121*(9), 6828–6845. https://doi.org/10.1002/2016JB012857

Liu, Y., & Rice, J. R. (2007). Spontaneous and triggered aseismic deformation transients in a subduction fault model. *Journal of Geophysical Research*, *112*(B9), B09404. https://doi.org/10.1029/2007JB004930.f

Liu, Y., & Rice, J. R. (2009). Slow slip predictions based on granite and gabbro friction data compared to GPS measurements in northern Cascadia. *Journal of Geophysical Research*, *114*(B9), B09407. https://doi.org/10.1029/2008JB006142

Mallick, R., Meltzner, A. J., Tsang, L. L. H., Lindsey, E. O., Feng, L., & Hill, E. M. (2021). Long-lived shallow slow-slip events on the Sunda megathrust. *Nature Geoscience*, *14*(5), 327–333. https://doi.org/10.1038/s41561-021-00727-y

Marone, C. (1998). Laboratory-derived friction laws and their application to seismic faulting. *Annual Review of Earth and Planetary Sciences*, *26*(1), 643–696. https://doi.org/10.1146/annurev.earth.26.1.643

Mase, C. W., & Smith, L. (1987). Effects of frictional heating on the thermal, hydrologic, and mechanical response of a fault. *Journal of Geophysical Research*, *92*(B7), 6249. https://doi.org/10.1029/JB092iB07p06249

Matsuzawa, T., Hirose, H., Shibazaki, B., & Obara, K. (2010). Modeling short-and long-term slow slip events in the seismic cycles of large subduction earthquakes. *Journal of Geophysical Research*, *115*(B12), B12301. https://doi.org/10.1029/2010JB007566

Matsuzawa, T., Shibazaki, B., Obara, K., & Hirose, H. (2013). Comprehensive model of short-and long-term slow slip events in the Shikoku region of Japan, incorporating a realistic plate configuration. *Geophysical Research Letters*, *40*(19), 5125–5130. https://doi.org/10.1002/grl.51006

McCaffrey, R., King, R. W., Payne, S. J., & Lancaster, M. (2013). Active tectonics of northwestern U.S. inferred from GPS-derived surface velocities. *Journal of Geophysical Research: Solid Earth*, *118*(2), 709–723. https://doi.org/10.1029/2012JB009473

Michel, S., Gualandi, A., & Avouac, J.-P. (2019). Similar scaling laws for earthquakes and Cascadia slow-slip events. *Nature*, *574*(7779), 522–526. https://doi.org/10.1038/s41586-019-1673-6

Miller, S. A. (2015). Modeling enhanced geothermal systems and the essential nature of large-scale changes in permeability at the onset of slip. *Geofluids*, *15*(1–2), 338–349. https://doi.org/10.1111/gfl.12108

Miyazaki, S., & Heki, K. (2001). Crustal velocity field of southwest Japan: Subduction and arc-arc collision. *Journal of Geophysical Research*, *106*(B3), 4305–4326. https://doi.org/10.1029/2000JB900312

Muñoz-Montecinos, J., Angiboust, S., Garcia-Casco, A., Glodny, J., & Bebout, G. (2021). Episodic hydrofracturing and large-scale flushing along deep subduction interfaces: Implications for fluid transfer and carbon recycling (Zagros Orogen, southeastern Iran). *Chemical Geology*, *571*, 120173. https://doi.org/10.1016/j.chemgeo.2021.120173

Nakajima, J., & Uchida, N. (2018). Repeated drainage from megathrusts during episodic slow slip. *Nature Geoscience*, *11*(5), 351–356. https://doi.org/10.1038/s41561-018-0090-z

Noda, H., Lapusta, N., & Kanamori, H. (2013). Comparison of average stress drop measures for ruptures with heterogeneous stress change and implications for earthquake physics. *Geophysical Journal International*, *193*(3), 1691–1712. https://doi.org/10.1093/gji/ggt074

Ohtani, M., & Hirahara, K. (2015). Effect of the Earth's surface topography on quasi-dynamic earthquake cycles. *Geophysical Journal International*, *203*(1), 384–398. https://doi.org/10.1093/gji/ggv187

Peacock, S. M., Christensen, N. I., Bostock, M. G., & Audet, P. (2011). High pore pressures and porosity at 35 km depth in the Cascadia subduction zone. *Geology*, *39*(5), 471–474. https://doi.org/10.1130/G31649.1

Perez-Silva, A., Kaneko, Y., Savage, M., Wallace, L., Li, D., & Williams, C. (2022). Segmentation of shallow slow slip events at the Hikurangi subduction zone explained by along-strike changes in fault geometry and plate convergence rates. *Journal of Geophysical Research: Solid Earth*, *127*(1), e2021JB022913. https://doi.org/10.1029/2021JB022913

Perez-Silva, A., Li, D., Gabriel, A.-A., & Kaneko, Y. (2021). 3D Modeling of long-term slow slip events along the flat-slab segment in the Guerrero Seismic Gap, Mexico. *Geophysical Research Letters*, *48*(13), e2021GL092968. https://doi.org/10.1029/2021GL092968

Perfettini, H., & Ampuero, J.-P. (2008). Dynamics of a velocity strengthening fault region: Implications for slow earthquakes and postseismic slip. *Journal of Geophysical Research*, *113*(B9), B09411. https://doi.org/10.1029/2007JB005398

Radiguet, M., Cotton, F., Vergnolle, M., Campillo, M., Walpersdorf, A., Cotte, N., & Kostoglodov, V. (2012). Slow slip events and strain accumulation in the Guerrero gap, Mexico. *Journal of Geophysical Research*, *117*(B4), B04305. https://doi.org/10.1029/2011JB008801

Radiguet, M., Perfettini, H., Cotte, N., Gualandi, A., Valette, B., Kostoglodov, V., et al. (2016). Triggering of the 2014 M_w 7.3 Papanoa earthquake by a slow slip event in Guerrero, Mexico. *Nature Geoscience*, *9*(11), 829–833. https://doi.org/10.1038/ngeo2817

Rice, J. R. (2006). Heating and weakening of faults during earthquake slip. *Journal of Geophysical Research*, *111*(B5), B05311. https://doi.org/10.1029/2005JB004006

Rubin, A. M., & Ampuero, J.-P. (2005). Earthquake nucleation on (aging) rate and state faults. *Journal of Geophysical Research*, *110*(B11), B11312. https://doi.org/10.1029/2005JB003686

Ruina, A. (1983). Slip instability and state variable friction laws. *Journal of Geophysical Research*, *88*(B12), 10359–10370. https://doi.org/10.1029/JB088iB12p10359

Sáez, A., Lecampion, B., Bhattacharya, P., & Viesca, R. C. (2022). Three-dimensional fluid-driven stable frictional ruptures. *Journal of the Mechanics and Physics of Solids*, *160*, 104754. https://doi.org/10.1016/j.jmps.2021.104754

Saffer, D. M., & Tobin, H. J. (2011). Hydrogeology and mechanics of subduction zone forearcs: Fluid flow and pore pressure. *Annual Review of Earth and Planetary Sciences*, *39*(1), 157–186. https://doi.org/10.1146/annurev-earth-040610-133408

Saffer, D. M., & Wallace, L. M. (2015). The frictional, hydrologic, metamorphic and thermal habitat of shallow slow earthquakes. *Nature Geoscience*, *8*, 594–600. https://doi.org/10.1038/ngeo2490

Schwartz, S. Y., & Rokosky, J. M. (2007). Slow slip events and seismic tremor at circum-Pacific subduction zones. *Reviews of Geophysics*, *45*(3), RG3004. https://doi.org/10.1029/2006RG000208

Segall, P., & Rice, J. R. (1995). Dilatancy, compaction, and slip instability of a fluid-infiltrated fault. *Journal of Geophysical Research*, *100*(B11), 22155–22171. https://doi.org/10.1029/95JB02403

Segall, P., Rubin, A. M., Bradley, A. M., & Rice, J. R. (2010). Dilatant strengthening as a mechanism for slow slip events. *Journal of Geophysical Research*, *115*(B12), B12305. https://doi.org/10.1029/2010JB007449

Shibazaki, B. (2003). On the physical mechanism of silent slip events along the deeper part of the seismogenic zone. *Geophysical Research Letters*, *30*(9), 1489. https://doi.org/10.1029/2003GL017047

Shibazaki, B., Obara, K., Matsuzawa, T., & Hirose, H. (2012). Modeling of slow slip events along the deep subduction zone in the Kii Peninsula and Tokai regions, southwest Japan. *Journal of Geophysical Research*, *117*(B6), B06311. https://doi.org/10.1029/2011JB009083

Shibazaki, B., & Shimamoto, T. (2007). Modelling of short-interval silent slip events in deeper subduction interfaces considering the frictional properties at the unstable—Stable transition regime. *Geophysical Journal International*, *171*(1), 191–205. https://doi.org/10.1111/j.1365-246X.2007.03434.x

Shibazaki, B., Wallace, L. M., Kaneko, Y., Hamling, I., Ito, Y., & Matsuzawa, T. (2019). Three-dimensional modeling of spontaneous and triggered slow-slip events at the Hikurangi subduction zone, New Zealand. *Journal of Geophysical Research: Solid Earth*, *124*(12), 13250–13268. https://doi.org/10.1029/2019JB018190

Sibson, R. H. (1990). Conditions for fault-valve behaviour. *Geological Society, London, Special Publications*, *54*(1), 15–28. https://doi.org/10.1144/GSL.SP.1990.054.01.02

Sibson, R. H. (1992). Fault-valve behavior and the hydrostatic-lithostatic fluid pressure interface. *Earth-Science Reviews*, *32*(1–2), 141–144. https://doi.org/10.1016/0012-8252(92)90019-P

Skarbek, R. M., & Rempel, A. W. (2016). Dehydration-induced porosity waves and episodic tremor and slip. *Geochemistry, Geophysics, Geosystems*, *17*(2), 442–469. https://doi.org/10.1002/2015GC006155

Stehfest, H. (1970). Numerical inversion of Laplace transforms. *Communications of the ACM*, *13*(1), 47–49. https://doi.org/10.1145/361953.361969

Takagi, R., Uchida, N., & Obara, K. (2019). Along-strike variation and migration of long-term slow slip events in the Western Nankai subduction zone, Japan. *Journal of Geophysical Research: Solid Earth*, *124*(4), 3853–3880. https://doi.org/10.1029/2019JB018037

Tan, Y. J., & Marsan, D. (2020). Connecting a broad spectrum of transient slip on the San Andreas fault. *Science Advances*, *6*(33), eabb2489. https://doi.org/10.1126/sciadv.abb2489

Tanaka, Y., Kato, A., Sugano, T., Fu, G., Zhang, X., Furuya, M., et al. (2010). Gravity changes observed between 2004 and 2009 near the Tokai slow-slip area and prospects for detecting fluid flow during future slow-slip events. *Earth Planets and Space*, *62*(12), 905–913. https://doi.org/10.5047/eps.2010.11.003

Tanaka, Y., Suzuki, T., Imanishi, Y., Okubo, S., Zhang, X., Ando, M., et al. (2018). Temporal gravity anomalies observed in the Tokai area and a possible relationship with slow slips. *Earth Planets and Space*, *70*(1), 25. https://doi.org/10.1186/s40623-018-0797-5

van Keken, P. E., Hacker, B. R., Syracuse, E. M., & Abers, G. A. (2011). Subduction factory: 4. Depth-Dependent flux of H_2O from subducting slabs worldwide. *Journal of Geophysical Research*, *116*(B1), B01401. https://doi.org/10.1029/2010JB007922

Wallace, L. M. (2020). Slow slip events in New Zealand. *Annual Review of Earth and Planetary Sciences*, *48*(1), 175–203. https://doi.org/10.1146/annurev-earth-071719-055104

Wallace, L. M., Beavan, J., McCaffrey, R., & Darby, D. (2004). Subduction zone coupling and tectonic block rotations in the North Island, New Zealand. *Journal of Geophysical Research*, *109*(B12), B12406. https://doi.org/10.1029/2004JB003241

Wallace, L. M., Webb, S. C., Ito, Y., Mochizuki, K., Hino, R., Henrys, S., et al. (2016). Slow slip near the trench at the Hikurangi subduction zone, New Zealand. *Science*, *352*(6286), 701–704. https://doi.org/10.1126/science.aaf2349

Wang, W., Savage, M. K., Yates, A., Zal, H. J., Webb, S., Boulton, C., et al. (2022). Temporal velocity variations in the northern Hikurangi margin and the relation to slow slip. *Earth and Planetary Science Letters*, *584*, 117443. https://doi.org/10.1016/j.epsl.2022.117443

Warren-Smith, E., Fry, B., Wallace, L., Chon, E., Henrys, S., Sheehan, A., et al. (2019). Episodic stress and fluid pressure cycling in subducting oceanic crust during slow slip. *Nature Geoscience*, *12*(6), 475–481. https://doi.org/10.1038/s41561-019-0367-x

Wech, A. G., & Bartlow, N. M. (2014). Slip rate and tremor Genesis in Cascadia. *Geophysical Research Letters*, *41*(2), 392–398. https://doi.org/10.1002/2013GL058607

Wibberley, C. A. J. (2002). Hydraulic diffusivity of fault gouge zones and implications for thermal pressurization during seismic slip. *Earth Planets and Space*, *54*(11), 1153–1171. https://doi.org/10.1186/BF03353317

Xue, L., Li, H.-B., Brodsky, E. E., Xu, Z.-Q., Kano, Y., Wang, H., et al. (2013). Continuous permeability measurements record healing inside the wenchuan earthquake fault zone. *Science*, *340*(6140), 1555–1559. https://doi.org/10.1126/science.1237237

Yang, Y., & Dunham, E. M. (2021). Effect of porosity and permeability evolution on injection-induced aseismic slip. *Journal of Geophysical Research: Solid Earth*, *126*(7), e2020JB021258. https://doi.org/10.1029/2020JB021258

Zal, H. J., Jacobs, K., Savage, M. K., Yarce, J., Mroczek, S., Graham, K., et al. (2020). Temporal and spatial variations in seismic anisotropy and V_p/V_s ratios in a region of slow slip. *Earth and Planetary Science Letters*, *532*, 115970. https://doi.org/10.1016/j.epsl.2019.115970

Zhu, W., Allison, K. L., Dunham, E. M., & Yang, Y. (2020). Fault valving and pore pressure evolution in simulations of earthquake sequences and aseismic slip. *Nature Communications*, *11*(1), 4833. https://doi.org/10.1038/s41467-020-18598-z